




**Implementation of self-consistent MGGA functionals in augmented plane wave based methods**Jan Doumont , Fabien Tran , and Peter Blaha *Institute of Materials Chemistry, Vienna University of Technology, Getreidemarkt 9/165-TC, A-1060 Vienna, Austria*

(Received 24 December 2021; revised 22 April 2022; accepted 2 May 2022; published 25 May 2022)

Functionals of the meta-generalized gradient approximation (MGGA) are widely used nowadays in chemistry and solid-state physics for the simulation of electronic systems such as molecules, solids, or surfaces. Due to their dependency on the kinetic energy density, they are in principle more accurate than GGA functionals for various properties (geometry, binding energy, electronic structure, etc.), while being nearly as fast since they are still of the semilocal form. Thus, when an accuracy better than GGA is required, one may consider using a MGGA instead of the much more costly hybrid functionals or methods such as the random-phase approximation or *GW*. In this work, the self-consistent implementation of MGGA functionals in augmented plane wave based methods is presented. Technical aspects of the implementation are discussed, and calculations of band gaps, lattice constants, and magnetic moments are presented in order to validate our implementation. To test the changes of the electron density due to a MGGA, the electric field gradient on transition-metal atoms is calculated.

DOI: [10.1103/PhysRevB.105.195138](https://doi.org/10.1103/PhysRevB.105.195138)**I. INTRODUCTION**

Kohn-Sham (KS) density functional theory (DFT) [1,2] is, in principle, an exact theory. However, in practice the exchange-correlation (xc) term in the total energy functional,  $E_{xc}$ , is treated approximately since a usable exact expression for the xc term has not been (and probably will never be) developed. Various classes of approximations for the xc energy functional  $E_{xc}$  and xc potential  $v_{xc}$  exist, and most of them belong to one of the rungs of Jacob's ladder of DFT [3,4]. Several hundreds of approximations have been proposed so far [5–7], and which one to choose for the problem at hand is not always obvious. The most simple approximation (the first rung of Jacob's ladder) for  $E_{xc}$  is the local density approximation (LDA) [2,8,9], where the xc energy density  $\epsilon_{xc}$  is a purely local functional of the electron density  $\rho$ ,  $E_{xc} = \int \epsilon_{xc}(\rho(\mathbf{r}))d^3\mathbf{r}$ . At the second rung of Jacob's ladder, there is the generalized gradient approximation (GGA) [10,11], where  $\epsilon_{xc}$  depends not only on the electron density  $\rho$ , but also on its first derivative  $\nabla\rho$ . Functionals of the meta-GGA (MGGA) type [12–14], at the third rung of Jacob's ladder, depend also on the noninteracting electronic kinetic energy density (KED)  $\tau$  and/or the Laplacian of the electron density  $\nabla^2\rho$ . At the fourth rung there are the functionals using the exact Hartree-Fock (HF) exchange, such as the hybrid functionals [15–17]. Finally, the functionals at the fifth rung also use the unoccupied Kohn-Sham orbitals (e.g., the random-phase approximation [18,19]).

Climbing up Jacob's ladder leads to functionals that should, in principle, be more accurate, but also more complicated to implement and computationally more expensive. Actually, the functionals of the fourth and fifth rungs are much more demanding in terms of computational time and memory. The functionals of the second and third rungs, the so-called semilocal functionals, are the most widely used, especially

in solid-state physics, where the GGA functionals have been the standard since the 1990s [11,20]. The past decade has seen a significant increase in popularity of MGGA [21] and hybrid [22] functionals. MGGA functionals are universally more accurate than GGAs; a MGGA can be quite accurate for both molecules and solids at the same time, while this is not possible with any GGA [23–27]. Hybrid functionals are particularly interesting for properties related to the electronic structure, such as the band gap [28–31].

The focus of the present work is on MGGA functionals. More specifically, the self-consistent implementation of KED-dependent MGGA functionals in augmented plane wave (APW) based methods will be presented. For this purpose, we made use of the WIEN2K code [32,33]. MGGA functionals have been implemented in a certain number of codes (see Refs. [12,34–47] for works reporting implementation details). However, in the literature there is no report of the self-consistent implementation of MGGA within the APW method [48–50]. We note that such an implementation is available in the ELK APW code [51]. The approach used in the ELK code differs significantly from ours, however. In their approach, the MGGA potential is added in a second-variational step, whereas in our approach it is added in the first variation.

Here, our goal is to derive the novel equations that arise from the KED-dependency in APW based methods, and to show that they are correctly implemented. We discuss the results for the band gap, lattice constant, and magnetic moment. As an application of MGGA functionals, the electric field gradient (EFG) on transition-metal atoms is calculated [52].

The paper is organized as follows. Section II gives details about the theory. Then, validation tests of the implementation are presented in Sec. III, while Sec. IV discusses the effect of self-consistency on the lattice constant. As an application of MGGA functionals, Sec. V presents the results for the EFG in systems with transition-metal atoms. The EFG is especially

suites as a benchmark because of its sensitive dependence on the electronic density  $\rho$ . Finally, Sec. VI summarizes the main points of this work.

## II. THEORY

### A. APW based methods

In the all-electron full-potential APW based methods, the unit cell is partitioned into two disjunct regions: nonoverlapping atomic spheres centered at the nuclei with radii  $R_{\text{at}}$ , and the interstitial region. Inside the spheres the orbitals, and all associated quantities (electron density, potential, etc.), are expanded in spherical harmonics  $Y_{\ell m}$ ; in the interstitial region, they are expanded in plane waves.

Within the spheres, a second partitioning is performed in low-energy core states and higher-energy valence (and semicore) states. The former are fully confined to the spheres (they have a vanishing wave function at and beyond the sphere boundary) and are obtained as atomiclike solutions of the Dirac equation with a (spherical) effective KS potential [53,54]. In this case, the variables can be separated in a radial and angular part in the usual way [55]. The core orbitals are thus given by radial functions multiplied by the spinor spherical harmonics:

$$\psi_{n\kappa m}^{\alpha}(\mathbf{r}) = \begin{pmatrix} g_{n\kappa m}(r)\xi_{\kappa m} \\ i f_{n\kappa m}(r)\xi_{-\kappa m} \end{pmatrix}, \quad (1)$$

where  $n$ ,  $\kappa$ , and  $m$  are the principal, relativistic, and magnetic quantum numbers, respectively.  $g_{n\kappa m}$  and  $f_{n\kappa m}$  are radial functions (large and small components, respectively) and  $\xi_{\kappa m}$  are the spinor spherical harmonics. The core states are calculated self-consistently, i.e., recalculated at each iteration of the self-consistency cycle. For spin-polarized cases, the effective potential has two components,  $v_{\text{KS}} = (v_{\text{KS}}^{\uparrow} \quad v_{\text{KS}}^{\downarrow})$ , such that the relativistic single-electron wave function has four components (large and small components for each spin). Spin mixing of the relativistic states is neglected. Note that the contribution from the core states to the KED is still defined from the positive-definite form of the nonrelativistic kinetic-energy operator [56]. This form must be used because (nonrelativistic) MGGA xc functionals are parametrized in terms of the nonrelativistic KED. For example, many MGGA functionals use the iso-orbital indicator  $\alpha_{\text{iso}} = (\tau - \tau^{\text{W}})/\tau^{\text{TF}}$  [where  $\tau^{\text{W}} = |\nabla\rho|/(8\rho)$  and  $\tau^{\text{TF}} = (3/10)(3\pi^2)^{2/3}\rho^{5/3}$  are the von Weizsäcker [57] and Thomas-Fermi [58,59] KED, respectively], assuming it has a lower bound of zero. For the nonrelativistic case, this is a safe assumption, because the KED  $\tau = \frac{1}{2} \sum_i \nabla\psi_i^* \cdot \nabla\psi_i$  is positive-definite. For the relativistic KED associated with the operator  $c\boldsymbol{\alpha} \cdot \hat{\mathbf{p}}$  [55,60], this is not guaranteed and this can lead to wrong results.

The valence states do extend over the whole unit cell and are described by (linearized) augmented plane waves [(L)APWs], depending on the case. As an illustration, the case of LAPW can trivially be generalized to APW basis functions, or functions describing semicore states [APW+lo, (high-derivative) local orbitals (HDLOs), etc.] [49,50,61–63].

The LAPW basis functions are given by

$$\phi_{\mathbf{K}}(\mathbf{r}) = \begin{cases} \sum_{\ell m} [A_{\alpha\ell m}^{\mathbf{K}} u_{\alpha\ell}(r_{\alpha}, E_{\alpha\ell}) + B_{\alpha\ell m}^{\mathbf{K}} \dot{u}_{\alpha\ell}(r_{\alpha}, E_{\alpha\ell})] Y_{\ell m}, & \mathbf{r} \in S_{\alpha}, \\ \frac{1}{\sqrt{\Omega}} e^{i\mathbf{K}\cdot\mathbf{r}}, & \mathbf{r} \in I, \end{cases} \quad (2)$$

where  $\mathbf{K} = \mathbf{k} + \mathbf{G}$  is the sum of the wave vector  $\mathbf{k}$  and the reciprocal-lattice vector  $\mathbf{G}$ ,  $\mathbf{r}_{\alpha} = \mathbf{r} - \mathbf{R}_{\alpha}$  is the distance from the nucleus  $\alpha$ , and  $\Omega$  is the volume of the unit cell. The radial function  $u_{\alpha\ell}$  and its energy derivative  $\dot{u}_{\alpha\ell}$  are constructed by integrating a spherical scalar-relativistic radial equation with the (spherically averaged) effective KS potential  $v_{\text{sp}}$  for a given energy parameter  $E_{\ell}$  [64]. Thus, the  $u_{\alpha\ell}$  are two-component functions, or four-component functions for spin-polarized cases. The matching coefficients  $A_{\alpha\ell m}^{\mathbf{K}}$  and  $B_{\alpha\ell m}^{\mathbf{K}}$  are determined by matching the value and slope of the large component to the plane wave [it is assumed that the small component is zero at the sphere boundary as the plane waves are nonrelativistic (one- or two-component) functions].

The addition of the energy derivative  $\dot{u}_{\alpha\ell}$  linearizes the radial basis with respect to the energy. This distinguishes LAPW from Slater's original APW method [65]. It is important to note for the discussion below that the contribution of  $B_{\alpha\ell m}^{\mathbf{K}} \dot{u}_{\alpha\ell}$  to the wave functions (and electron density) is a measure of the quality of the basis set. It should be much smaller than the contribution from  $A_{\alpha\ell m}^{\mathbf{K}} u_{\alpha\ell}$ ; otherwise it is an indication that the energy parameter  $E_{\alpha\ell}$  or the atomic radius  $R_{\text{at}}^{\alpha}$  may be badly chosen.

An important addition to the basis set are local orbitals (LOs) [66]; these are linear combinations of LAPW radial functions with a third radial function  $C_{\alpha\ell m}^i u_{\alpha\ell}(r_{\alpha}, E_{\ell i}^{\alpha})$  with another (often semicore) energy parameter  $E_{\ell i}^{\alpha}$ . Provided the energy parameters are properly chosen (far enough apart), multiple LOs, indexed  $i$ , could be added per atom and per azimuthal quantum number  $\ell$ . They are defined to be zero in the interstitial region, and the coefficients  $A_{\alpha\ell m}^i$ ,  $B_{\alpha\ell m}^i$ , and  $C_{\alpha\ell m}^i$  are chosen such that the linear combination is normalized and has zero value and slope at the atomic sphere boundary.

Another linearization scheme is the APW+lo basis. It uses the LO concept to eliminate the explicit energy dependence of the APW basis functions. For a detailed discussion of this approach, see Refs. [61,62].

However, all approaches boil down to linear combinations of radial functions. For generality and simplicity of the notation, in the following we will write basis functions using  $\phi_{\mu}$  to indicate either an extended (L)APW or a local orbital (LO/lo) basis function, and the associated (linear combination of) radial functions simply as  $f_{\mu\ell m}$ ;  $\mu$  is a shorthand index for, as applicable, the atom index  $\alpha$ , lo index  $i$ , and wave number  $\mathbf{K}$ . Unless necessary, we will also mute the spin index  $\sigma$  (however, all equations are given in the spin-polarized form), the atomic index  $\alpha$ , as well as the  $r$  and  $\hat{\mathbf{r}}$  dependencies of functions in most equations.

### B. Meta-generalized gradient approximation

As mentioned in Sec. I, KED-dependent MGGA functionals

$$E_{\text{xc}} = \int_{\text{cell}} \epsilon_{\text{xc}}(\rho_{\uparrow}, \rho_{\downarrow}, \nabla\rho_{\uparrow}, \nabla\rho_{\downarrow}, \tau_{\uparrow}, \tau_{\downarrow}) d^3\mathbf{r} \quad (3)$$

depend on the electron density

$$\rho_\sigma = \underbrace{\sum_{nk} w_{nk}^\sigma |\psi_{nk}^\sigma|^2}_{\rho_\sigma^{\text{val}}} + \underbrace{\sum_{\alpha nk m} |\psi_{nk m}^{\alpha\sigma}|^2}_{\rho_\sigma^{\text{core}}}, \quad (4)$$

its first derivative  $\nabla \rho_\sigma$ , and the noninteracting positive-definite KED,

$$\tau_\sigma = \underbrace{\frac{1}{2} \sum_{nk} w_{nk}^\sigma \nabla \psi_{nk}^{\sigma*} \cdot \nabla \psi_{nk}^\sigma}_{\tau_\sigma^{\text{val}}} + \underbrace{\frac{1}{2} \sum_{\alpha nk m} \nabla \psi_{nk m}^{\alpha\sigma*} \cdot \nabla \psi_{nk m}^{\alpha\sigma}}_{\tau_\sigma^{\text{core}}}, \quad (5)$$

where  $w_{nk}^\sigma$  is the product of the  $\mathbf{k}$ -point weight and occupation number. Note that this positive-definite KED is different from the KED that is derived from the sum of eigenvalues in all-electron methods [56,67].

Since Eq. (3) depends on  $\tau_\sigma$ , it is not an explicit functional of the density  $\rho_\sigma$ , like LDA and GGA functionals. Therefore, the xc potential  $v_{xc,\sigma}$ , which is defined as the functional derivative of  $E_{xc}$  with respect to the density ( $v_{xc,\sigma} = \delta E_{xc} / \delta \rho_\sigma$ ), cannot be calculated straightforwardly, but only via the optimized effective potential (OEP) method [68]. The OEP equations are often solved approximately by using the Krieger-Li-Iafate simplification [69] of the OEP method (see Refs. [37,42,43]). Therefore, in most implementations, the corresponding potential of Eq. (3) is calculated within the generalized KS [70] (gKS) framework by taking the functional derivative with respect to the KS orbital  $\psi_i^\sigma$  (Ref. [34]):

$$\begin{aligned} \hat{v}_{xc,\sigma} \psi_i^\sigma &= \frac{\delta E_{xc}}{\delta \psi_i^{\sigma*}} \\ &= \left( \frac{\partial \epsilon_{xc}}{\partial \rho_\sigma} - \nabla \cdot \frac{\partial \epsilon_{xc}}{\partial \nabla \rho_\sigma} \right) \psi_i^\sigma \\ &\quad - \frac{1}{2} \nabla \cdot \left( \frac{\partial \epsilon_{xc}}{\partial \tau_\sigma} \nabla \psi_i^\sigma \right). \end{aligned} \quad (6)$$

In Eq. (6), the term in the large parentheses,  $v_{xc,\sigma}^{\text{mult}} = \partial \epsilon_{xc} / \partial \rho_\sigma - \nabla \cdot (\partial \epsilon_{xc} / \partial \nabla \rho_\sigma)$ , has the same form as a GGA potential  $v_{xc,\sigma}^{\text{GGA}} = \partial \epsilon_{xc}^{\text{GGA}} / \partial \rho_\sigma - \nabla \cdot (\partial \epsilon_{xc}^{\text{GGA}} / \partial \nabla \rho_\sigma)$  and is multiplicative. The expanded formula for this term can be found in Appendix A. The last term in Eq. (6) arises due to the KED-dependency of Eq. (3) and consists of a non-multiplicative operator  $\hat{v}_{\tau,\sigma} = (-1/2) \nabla \cdot (v_{\eta,\sigma} \nabla)$ , where for conciseness we define  $v_{\eta,\sigma} = \partial \epsilon_{xc} / \partial \tau_\sigma$ .

### C. Hamiltonian matrix element

It is in principle straightforward to calculate the Hamiltonian matrix elements in a gKS approach, namely by applying the operator  $\hat{v}_\tau$  on a basis function  $\phi_\nu$  and multiplying on the left with another basis function  $\phi_\mu$ . In the LAPW method, however, the basis functions themselves depend on the potential, and the gKS approach cannot be applied to the construction of the radial basis functions (nor to the core electrons) because they are calculated by direct integration.

If a radial equation (relativistic or not) is integrated using a nonmultiplicative potential, the solutions are in general not orthogonal. Therefore, we use an appropriate GGA xc potential for this step.

We note that it may be possible to use an OEP (or an approximation thereof) during this step, while keeping the gKS scheme to compute the matrix elements. This lies outside the scope of this paper, however.

This approach has some limitations. First, if the GGA potential is not well-chosen, the quality of the (radial) basis functions is diminished. In practice (as will be shown in Sec. III) this is rarely an issue. A previous work has already shown that the OEP  $v_{xc}$  of SCAN only differs in small details from the potential  $v_{xc}$  of PBE [43]. If problems do occur due to poor basis functions, this can be detected. In this case (which can occur also in typical KS calculations, for example when energy parameters are badly chosen) the charge contribution coming from the linearizing term  $\hat{u}_{\alpha\ell}$  becomes large. Our code then produces a warning automatically. Examples of this will be discussed in Sec. III.

Secondly, because the core and valence electrons are treated using inconsistent potentials (which are not the functional derivative of a single energy functional), the calculation of forces is in principle not possible. Note that the valence electrons are still treated fully consistently with the MGGA potential in the gKS scheme.

The GGA xc potential for the core electrons and radial functions  $f_{\mu\ell m}$  was chosen according to the variational principle. In Ref. [71], the band gap of solids was calculated non-self-consistently (from total-energy calculations) with a MGGA, but using GGA orbitals. It was shown that the variationally optimal GGA orbitals (those giving the lowest total MGGA energy) are also the ones that lead to the most correct MGGA band gaps, which is rather expected. For the present work, it was found that the best GGA potential to use in the construction of the basis functions is the same as those that were determined in Ref. [71] to be the best for non-self-consistent MGGA calculations (and in the subsequent work [72]), namely RPBE [73] (for TPSS [13] and SCAN [21]), mRPBE [71] (for HLE17 [74]), and HCTH/407 [75] (for TASK [76]).

Note that using only the multiplicative part of the MGGA potential in this step is not possible. The contribution from the nonmultiplicative part to the total potential in Eq. (6) is so large that the remaining multiplicative part is a very poor approximation, much worse than a standard GGA potential. Ignoring the nonmultiplicative part in this step would introduce large errors in the core density and the radial functions.

With the basis set fully determined, we can set up the secular equation to solve the gKS eigenvalue problem  $\hat{H} \psi_n = \epsilon_n \psi_n$ . The overlap matrix  $S$  is unaffected by the choice of the potential. It is natural in APW based methods to consider the spherical part of the Hamiltonian separately from the non-spherical part and the interstitial part. For a MGGA potential in the gKS scheme, a third contribution is given by the matrix elements of the KED-derived operator  $\hat{v}_\tau$ :

$$\hat{H} = \hat{H}_I + \hat{H}_{\text{sp}} + v_{\text{ns}} + \hat{v}_{\text{ns},\tau}. \quad (7)$$

In APW based methods, the contribution of the spherical part  $\hat{H}_{\text{sp}}$  to the matrix elements is fully determined by the energy

parameters  $E_l$  and orthonormality of the radial functions. The (atomic) nonspherical and KED-dependent contributions are calculated through numerical integration. The first two terms are discussed in the literature [49]; we only note that a correction must be added to the spherical part to account for the difference between the GGA used to construct the radial functions and the multiplicative part of the MGGA:

$$\langle \phi_\mu | \hat{H}_{\text{sp}} | \phi_\nu \rangle = \langle \phi_\mu | \hat{H}_{\text{sp}}^{\text{GGA}} | \phi_\nu \rangle + \langle \phi_\mu | v_{\text{sp}}^{\text{mult}} - v_{\text{sp}}^{\text{GGA}} | \phi_\nu \rangle, \quad (8)$$

where  $v_{\text{sp}}^{\text{mult}}$  and  $v_{\text{sp}}^{\text{GGA}}$  are the spherical components of the multiplicative part of the potential and the auxiliary GGA potential, respectively. The first term on the right-hand side of Eq. (8) is still only dependent on the energy parameters, whereas the second term is calculated by numerical integration.

The KED-derived gKS contribution  $\langle \phi_\mu | \hat{v}_\tau | \phi_\nu \rangle$  is evaluated using integration by parts:

$$\begin{aligned} \langle \phi_\mu | \hat{v}_\tau | \phi_\nu \rangle &= \frac{1}{2} \left[ \sum_\alpha \int_{S_\alpha} + \int_I \right] v_\eta \nabla \phi_\mu^* \cdot \nabla \phi_\nu d^3 \mathbf{r} \\ &\quad - \frac{1}{2} \sum_\alpha \oint_{\partial S_\alpha} v_\eta \phi_\mu^* (\nabla \phi_\nu) \cdot \hat{\mathbf{r}} d\Omega \end{aligned} \quad (9)$$

and their detailed form for APW based basis functions can be found in Appendix B.

With the Hamiltonian and overlap matrices determined, the secular equation can be solved. It provides the KS orbitals, from which the electron density and the KED are determined, closing the self-consistency loop.

#### D. Total energy

The total energy per unit cell is given by

$$\begin{aligned} E_{\text{tot}} &= T_s + \frac{1}{2} \int_{\text{cell}} v_{\text{Coul}}(\mathbf{r}) \rho(\mathbf{r}) d^3 \mathbf{r} \\ &\quad - \frac{1}{2} \sum_\alpha Z_\alpha v_M^\alpha(\mathbf{R}_\alpha) + E_{\text{xc}}, \end{aligned} \quad (10)$$

where  $T_s$  is the kinetic energy of the electrons, and

$$v_{\text{Coul}}(\mathbf{r}) = \int_{\text{cell}} \frac{\rho(\mathbf{r}')}{|\mathbf{r} - \mathbf{r}'|} d^3 \mathbf{r}' - \sum_\beta \frac{Z_\beta}{|\mathbf{r} - \mathbf{R}_\beta|}, \quad (11)$$

$$v_M^\alpha(\mathbf{R}_\alpha) = \int_{\text{cell}} \frac{\rho(\mathbf{r}')}{|\mathbf{R}_\alpha - \mathbf{r}'|} d^3 \mathbf{r}' - \sum_{\beta \neq \alpha} \frac{Z_\beta}{|\mathbf{R}_\alpha - \mathbf{R}_\beta|} \quad (12)$$

are the Coulomb and Madelung potentials, respectively ( $Z_\alpha$  is the charge of nucleus  $\alpha$ ). By using the sum of the eigenvalues,  $E_{\text{tot}}$  can be rewritten for a MGGA functional in the gKS scheme as

$$\begin{aligned} E_{\text{tot}} &= \sum_{\alpha \sigma n k m} \epsilon_{nk m}^{\alpha \sigma} + \sum_{\sigma n k} w_{nk}^\sigma \epsilon_{nk}^\sigma + E_{\text{xc}}^{\text{MGGA}} \\ &\quad - \frac{1}{2} \int_{\text{cell}} v_{\text{Coul}}(\mathbf{r}) \rho(\mathbf{r}) d^3 \mathbf{r} - \frac{1}{2} \sum_\alpha^{\text{cell}} Z_\alpha v_M^\alpha(\mathbf{R}_\alpha) \end{aligned}$$

$$\begin{aligned} &- \sum_\sigma \int_{\text{cell}} v_{\text{xc}, \sigma}^{\text{GGA}}(\mathbf{r}) \rho_\sigma^{\text{core}}(\mathbf{r}) d^3 \mathbf{r} \\ &- \sum_\sigma \int_{\text{cell}} v_{\text{xc}, \sigma}^{\text{mult}}(\mathbf{r}) \rho_\sigma^{\text{val}}(\mathbf{r}) d^3 \mathbf{r} \\ &- \sum_\sigma \int_{\text{cell}} v_{\eta, \sigma}(\mathbf{r}) \tau_\sigma^{\text{val}}(\mathbf{r}) d^3 \mathbf{r}, \end{aligned} \quad (13)$$

where  $v_{\text{xc}, \sigma}^{\text{GGA}}$  is the GGA potential used for the core electrons (as well as for the calculation of the radial functions  $f_{\mu l m}$ ). Except for the addition of the last KED-derived term, and the separation of the core and valence potentials, this expression is equivalent to the one given by Weinert *et al.* [67] for the KS scheme.

#### E. Computational details

As already mentioned, the WIEN2K code [32,33] is used for the present study. In the self-consistent implementation of MGGA functionals, the xc energy density  $\epsilon_{\text{xc}}$  and its derivatives with respect to  $\rho_\sigma$  and  $\tau_\sigma$  are provided by the library of xc functionals Libxc [5,6].

An overview of the required parameters to reach the same convergence level for PBE, SCAN, HLE17, and TASK is listed in Table I.  $G_{\text{max}}$  is the cutoff for the Fourier coefficients of quantities (density, KED, and potentials) in the interstitial (and thus the size of the Fourier grids), whereas  $R_{\text{min}}^{\text{at}} K_{\text{max}}$  is the product of the plane-wave basis cutoff and the smallest atomic sphere in the system. Other parameters like the  $\mathbf{k}$ -mesh and cutoffs of the spherical harmonics expansions were found to be unaffected by the choice between a MGGA or a GGA functional.

It is clear that SCAN and TASK require a larger Fourier cutoff  $G_{\text{max}}$ . This applies to a lesser extent to HLE17. The required plane-wave cutoff is not significantly affected (though there are some fluctuations), except for LiF. LiF is a special case however, as it has no core states, and a convergence of 0.01 eV in the band gap (considering the predicted band gap of 12.58 eV with TASK) is a quite strict convergence criterion.

On the basis of these results, a  $G_{\text{max}}$  of 24 should be safe for all or most MGGAs, compared to 12 for PBE (although 14 is the default setting in WIEN2K). Because SCAN is so numerically demanding, regularized versions have been developed [77,78]. These should have better convergence behavior. Depending on the MGGA functional that is chosen and the system under consideration, we expect that in most cases a lower value can be used for  $G_{\text{max}}$ . The choice for basis set size (which is the most important parameter with respect to computational time as it determines the size of the Hamiltonian matrix) is not affected by MGGAs compared to PBE.

In Table II, we list the timings for five systems. Three of them—Al<sub>2</sub>O<sub>3</sub>, Si, and Zn—will be discussed below. The other two systems have been chosen to include also more computationally demanding cases. MoS<sub>2</sub> is a well-known transition-metal monolayer, and calculations including MGGAs were published in Ref. [79]. The last system is a supercell of Ge with an interstitial defect. It contains 129

TABLE I. Parameters required to converge the total energy to 0.01 Ry, band gaps to 0.01 eV, EFG to  $0.01 \cdot 10^{21}$  V/m<sup>2</sup>, and magnetic moment to  $0.01 \mu_B$ . The column names  $G$  and  $K$  are short for the parameters  $G_{\max}$  and  $R_{\min}^{\text{at}} K_{\max}$  as defined in the text.

Solid	PBE		TPSS		SCAN		TASK		HLE17	
	$G$	$K$	$G$	$K$	$G$	$K$	$G$	$K$	$G$	$K$
Al <sub>2</sub> O <sub>3</sub>	12	8.0	12	8.0	20	8.0	20	8.5	12	8.0
LiF	12	6.0	16	7.0	16	6.0	20	8.0	16	7.0
Ru	12	9.0	12	8.5	16	9.0	16	9.0	12	9.0
Si	12	7.0	12	7.0	12	7.0	12	7.0	12	7.0
Zn	12	8.5	12	9.0	24	9.0	12	9.0	12	9.0
NiO	12	8.0	12	8.0	22	8.0	12	7.5	12	8.0
MoS <sub>2</sub>	10	7.0	10	7.0	10	7.0	10	7.0	14	7.0
Ge	12	8.0	12	8.0	12	8.0	12	8.0	12	8.0

atoms in the unit cell, and it was discussed in Ref. [80] (not including MGGA calculations).

We show timings for PBE, PBE using the recommended MGGA parameters, and SCAN. This way, the influence of the parameters can be separated from the computational complexity that is intrinsic to the MGGAs. For TPSS, TASK, and HLE17 we show just the timing for the construction of the potential and number of self-consistency iterations required, as the other timings are indistinguishable.

The largest influence is obviously on the calculation of the potential. The doubling of  $G_{\max}$  implies that the Fourier grid will be eight times larger. Additionally, a second Fourier grid must be stored in memory for the KED-dependent part of the potential. This is reflected clearly in the timings, where one

sees a large jump when doubling  $G_{\max}$  using PBE. The additional complexity introduced by using a MGGA is a factor of 2–3, depending on the chosen functional. In general, HLE17 takes the longest to evaluate, followed by TPSS, SCAN, and finally TASK. The lower relative complexity of TASK might be explained by the fact that only the exchange part is a MGGA (the correlation is taken from LDA). It is interesting to note that for MoS<sub>2</sub> the relative order of SCAN and TPSS is reversed. This is probably caused by the presence of vacuum regions in this case, combined with the piecewise definitions of the functionals. It is hard to track down the exact cause, however, due to the complexity of the definitions of the functionals and the impact of compiler optimizations. Overall the main impact comes from the parameter  $G_{\max}$ , for which we

TABLE II. Timings per iteration (in seconds), and number of iterations needed from an initial superposition of atomic densities, for four benchmark systems using PBE, SCAN, TPSS, TASK, and HLE17. We performed all calculations sequentially (i.e., on a single core) on an Intel i7-7820X CPU (eight cores @ 3.60 GHz), except the Ge (d) case, which was parallelized using MPI across all cores of two identical machines.  $R_{\min}^{\text{at}} K_{\max}$  was chosen the same for all functionals and according to the values listed in Table I: 7.0 for Si and MoS<sub>2</sub>, 8.0 for Ge and Al<sub>2</sub>O<sub>3</sub>, and 9.0 for Zn. The timings for one iteration have been separated into the calculation of the potential  $V$ , the setup and diagonalization of the Hamiltonian matrix, and “other” (calculation of density, KED, mixing, and core states). For MoS<sub>2</sub>, spin-orbit coupling was included, which explains the larger amount of time spent in “other.” The asterisk for the number of iterations for MoS<sub>2</sub> using TASK signifies that this case was restarted from a converged SCAN calculation.

Functional	Step	Si	Zn	Al <sub>2</sub> O <sub>3</sub>	MoS <sub>2</sub>	Ge (d)
PBE ( $G_{\max} = 12$ )	$V$	1	<1	1	2	44
	$H$	2	7	172	38	882
	other	2	4	57	87	287
	iter. no.	9	9	8	11	13
PBE ( $G_{\max} = 24$ )	$V$	7	3	6	8	334
	$H$	2	7	176	38	874
	other	2	4	57	85	295
	iter. no.	9	9	8	11	13
SCAN ( $G_{\max} = 24$ )	$V$	15	4	14	25	605
	$H$	2	7	227	41	885
	other	2	4	56	82	297
	iter. no.	9	10	12	11	15
TPSS ( $G_{\max} = 24$ )	$V$	19	6	17	23	626
	iter. no.	9	9	10	11	14
TASK ( $G_{\max} = 24$ )	$V$	13	4	11	18	581
	iter. no.	9	11	11	65*	15
HLE17 ( $G_{\max} = 24$ )	$V$	22	6	19	26	634
	iter. no.	9	11	11	11	17

chose for the timings a very high value (compare with the actual necessary  $G_{\max}$  as given in Table I). For very intensive cases, it will often be possible to reduce this parameter depending on the composition of the system and functional used, e.g., after testing the convergence on a smaller system with similar composition or physical features.

The setup and diagonalization are only modestly affected. In fact, the diagonalization should be exactly as expensive, as the Hamiltonian matrix has the same dimensions. The change in this step comes almost entirely from the calculation of the spherical terms [see Eq. (B14)], which takes about 50% longer. The setup has a computational complexity of  $O(N^2)$ , but for the diagonalization it is  $O(N^3)$ , thus the difference between the timings for this step will tend to zero for larger cases.

In the last category “other,” there are very small differences, which can be traced back to the construction and mixing of the positive-definite KED  $\tau$  (which we implemented similarly to Ref. [56]).

The number of iterations needed was unchanged, or only modestly increased. The exception was the calculation of MoS<sub>2</sub> with TASK, where 65 iterations were needed starting from a converged PBE calculation (compared to the others, which are started from a superposition of atomic densities). This shows that, in some cases, convergence with gKS MGGA can be tricky for 2D systems (and probably also other systems including vacuum regions). The authors also experienced this for the calculation presented in Ref. [79]. However, we did not observe such issues in bulk systems.

On the whole, we see that the computational expense of a MGGA calculation using our implementation is not much higher than that of a GGA calculation. On a few points, there are probably still optimizations possible. Notably, the mixing of the density in our code is done using a sophisticated optimization scheme [81], whereas the KED is mixed independently according to a simple ‘Pratt’ scheme, where the current and previous KED are simply added with a fixed non-adaptive proportion and scaled. Possibly an improved mixing scheme could solve the slow convergence found for some cases with vacuum regions.

### III. VALIDATION OF THE IMPLEMENTATION

#### A. Band gap

To check the correctness of our implementation of the MGGA potential, we consider the band gap of a set of solids. By band gap, we mean the difference between the eigenvalues  $\epsilon_{nk}$  at the valence-band maximum (VBM) and the conduction-band minimum (CBM):

$$E_g^{(g)KS} = \epsilon_{CBM}^{(g)KS} - \epsilon_{VBM}^{(g)KS}, \quad (14)$$

which is, here for MGGA functionals, applied in the gKS framework. At this point, it is worth mentioning a few things about the xc derivative discontinuity  $\Delta_{xc}$  [84,85].  $\Delta_{xc}$  is defined as

$$\Delta_{xc} = E_g^{I-A} - E_g^{KS}, \quad (15)$$

where  $E_g^{I-A} = I - A$  is the true band gap calculated as the difference between the ionization potential  $I$  and electron affinity  $A$  of the system, and  $E_g^{KS}$  is calculated with Eq. (14)

when the potential is implemented in the KS framework so that it is multiplicative. For solids, LDA and GGA functionals lead to  $\Delta_{xc} = 0$  (see Refs. [86,87]), which is the main reason why LDA/GGA strongly underestimate the band gap with respect to experiment [31,88] (note, however, that a few less common GGA functionals [89–91] lead to much better band gaps, although  $\Delta_{xc}$  is still zero). Functionals that lead to a nonmultiplicative gKS potential, like MGGA and HF/hybrids, possess a nonzero xc derivative discontinuity  $\Delta_{xc}$  [92]. With such nonmultiplicative gKS potentials,  $\Delta_{xc}$  is included in  $E_g^{gKS}$  (see Refs. [92–94]), and consequently  $E_g^{gKS}$  is usually in better agreement with the experimental value of  $E_g^{I-A}$ , as shown in numerous benchmark studies [31,70,76,82,83,91,95,96]. It is also interesting to note that the derivative discontinuity  $\Delta_{xc}$  is not included in the CBM-VBM difference when the MGGA potential is implemented using the OEP method, however  $\Delta_{xc}$  is in principle nonzero and can be calculated [43].

Among the numerous proposed MGGA functionals [14], HLE17 [74] and TASK [76] are some of the most accurate for the band gap of solids [albeit they are slightly less accurate than the modified Becke-Johnson (mBJ) MGGA potential [97–99], as shown in Ref. [83]]. Therefore, they are of particular interest for testing our implementation of MGGA potentials. Also considered are the well-known TPSS [13] and SCAN [21], the latter being very successful for total energy calculations [100,101]. While TPSS leads basically to no improvement with respect to PBE [11] for the band gap, SCAN is clearly more accurate, but not as much as HLE17 or TASK [83,102].

The results for the band gap of 30 solids obtained with the WIEN2K code are shown in Table III. This set of solids is the one that we used in Ref. [71] for the non-self-consistent calculation of the band gap with MGGA functionals using the total energy  $E_{\text{tot}}$ . It is a subset of the much larger set of 473 solids built by Borlido *et al.* [82,83,103]. The results are compared with the results from Refs. [82,83], which were obtained with the VASP code [104] that uses the projector augmented wave (PAW) formalism [105,106]. The agreement between the two codes can be considered as satisfying, since in the majority of cases the difference  $E_g^{\text{WIEN2K}} - E_g^{\text{VASP}}$  between the two codes is below 0.05 eV. The mean absolute difference (MAD) is 0.03 and 0.04 eV for TPSS and SCAN, respectively, but slightly larger for HLE17 and TASK (0.06 and 0.07 eV, respectively). The mean differences (MD) for all functionals are much smaller, showing there is no systematic error. The mean absolute percentage deviation (MAPD) for the MGGA functionals varies between 1.4% and 2.4%, which is much smaller than that for PBE. The MAPD of 4.2% of PBE, however, is dominated by the very large relative difference of 88% for Ge. From such small MADs and MAPDs between WIEN2K and VASP, we can conclude that the new implementation of the MGGA potentials in WIEN2K is correct and accurate.

For AlSb, we did not use the result from Refs. [82,83] as we found a significant discrepancy between the results. We found a value of 2.15 eV (WIEN2K), compared to their result of 2.87 eV (VASP). Therefore, we recalculated this case ourselves with VASP and found a value of 2.07 eV, in good agreement with WIEN2K. Additionally, we confirmed that our VASP result can be reproduced using different pseudopotentials. Our

TABLE III. Band gaps (in eV) calculated with MGGA functionals using the WIEN2K code at experimental lattice parameters. The columns  $\Delta$  show the difference with respect to the VASP result ( $E_g^{\text{WIEN2K}} - E_g^{\text{VASP}}$ ) from Refs. [82,83] (except AlSb, which we calculated ourselves; see the text). For comparison, the PBE results are also shown.

Solid	PBE	$\Delta$	TPSS	$\Delta$	SCAN	$\Delta$	HLE17	$\Delta$	TASK	$\Delta$
Al <sub>2</sub> O <sub>3</sub>	6.20	0.01	6.35	0.04	7.08	0.04	7.12	0.17	8.70	-0.01
AlAs	1.47	0.04	1.53	0.04	1.77	0.04	2.53	0.04	2.49	0.05
AlN	4.14	-0.00	4.14	0.00	4.79	0.00	4.79	0.05	5.77	-0.08
AlP	1.59	0.01	1.66	0.02	1.91	0.01	2.73	-0.06	2.45	-0.01
AlSb	1.22	0.01	1.28	0.01	1.37	0.00	1.94	0.14	2.15	0.08
Ar	8.71	-0.01	9.37	0.06	9.63	0.13	10.90	0.06	13.21	-0.06
BeO	7.37	0.02	7.39	0.06	8.21	0.05	8.51	0.04	9.59	-0.04
BN	4.46	0.01	4.49	0.06	4.96	0.03	5.73	0.04	5.42	0.02
BP	1.25	-0.02	1.29	-0.02	1.53	-0.05	2.16	-0.07	1.48	-0.02
C	4.14	-0.01	4.17	-0.02	4.54	-0.03	5.01	0.01	4.33	-0.00
CaF <sub>2</sub>	7.28	0.00	7.76	0.03	7.88	0.05	9.38	0.04	10.45	0.03
CaO	3.67	0.04	3.79	0.04	4.24	0.08	4.54	0.03	5.16	-0.08
CdSe	0.71	-0.04	0.90	-0.00	1.11	0.04	1.67	-0.06	2.11	0.00
GaAs	0.52	-0.05	0.68	-0.00	0.78	-0.02	0.75	0.09	1.72	0.05
GaP	1.59	-0.05	1.64	-0.04	1.83	-0.05	2.22	0.02	2.37	-0.01
Ge	0.06	-0.05	0.18	0.01	0.18	0.04	0.00	0.00	0.89	0.02
InP	0.68	-0.03	0.82	0.00	1.04	-0.01	1.10	-0.02	1.87	-0.21
KCl	5.21	-0.00	5.73	0.01	5.84	0.06	6.91	-0.01	8.72	-0.04
Kr	7.26	-0.01	7.89	-0.00	8.03	-0.01	9.30	-0.01	11.37	-0.11
LiCl	6.33	0.00	6.57	0.02	7.28	0.10	7.79	0.02	9.50	0.04
LiF	9.08	0.00	9.25	-0.01	9.97	-0.01	10.81	-0.01	12.76	0.16
LiH	3.03	0.03	3.44	0.08	3.63	-0.01	4.75	0.13	5.48	0.05
MgO	4.71	0.00	4.83	0.03	5.58	0.05	5.70	0.09	7.25	-0.06
NaCl	5.11	0.01	5.49	0.04	5.89	0.04	6.78	0.07	8.66	-0.04
NaF	6.33	0.02	6.75	0.07	7.04	0.02	8.41	0.12	10.32	-0.04
Ne	11.58	-0.00	12.17	0.02	12.90	0.13	14.29	0.03	16.98	-0.01
Si	0.58	-0.04	0.66	-0.04	0.83	-0.04	1.56	-0.07	1.00	-0.02
SiC	1.36	0.01	1.38	0.06	1.68	-0.03	2.34	0.05	1.95	-0.03
ZnO	0.82	0.02	0.76	0.03	1.18	0.04	2.22	-0.16	2.04	-0.04
ZnS	2.12	-0.03	2.28	-0.01	2.63	0.00	3.18	-0.11	3.77	-0.02
MD	0.00		-0.02		-0.02		-0.02		0.04	
MAD	0.02		0.03		0.04		0.06		0.07	
MAPD	4.2 %		1.4 %		2.1 %		2.1 %		2.4 %	

WIEN2K result is also independent of various parameters such as the choice of LAPW or APW+lo basis, putting the Sb 4s and 4p orbitals in core or valence, the sphere size, as well as the choice of the local GGA potential (as indicated in Table IV).

In a recent study [103], the band gaps of the aforementioned 473 solids were calculated with three DFT codes, namely WIEN2K, VASP, and ABINIT [107], and compared. The goal was to estimate the error in the band gap induced by using an inconsistent pseudopotential (PP) or PAW-setup, like, for instance, using a LDA or PBE PP/PAW-setup for a calculation with another functional. The WIEN2K results were used as reference. When a consistent PP/PAW-setup is used, the MAD between WIEN2K and VASP/ABINIT is 0.02–0.03 eV, which is very small. However, the MAD increases up to  $\sim 0.1$  eV when a LDA or PBE PP/PAW-setup is used for a calculation with a very different functional like HLE16 [91], Sloic [90], or mBJ. Considering this, the MADs obtained here for the MGGA are very reasonable, including HLE17 and TASK, which are by construction very different from more standard functionals like TPSS or SCAN.

As discussed in Sec. II B, the MGGA potential is not implemented in the atomic codes that are used to calculate the core orbitals and the radial functions of the basis set. Thus, a GGA potential has to be used instead. This may lead to a suboptimal core density and/or basis set in the spheres. However, the variational principle guarantees that the lowest total energy corresponds to the best core density and basis set. Following these principles, the optimal GGA potential is RPBE for TPSS and SCAN, mRPBE for HLE17, and HCTH/407 for TASK [71]. To illustrate the effect of the GGA potential used in the atomic codes on the band gap, the calculations were repeated by using the PBE GGA potential instead, and Table IV shows the difference with respect to the results in Table III. The effect is absolutely negligible in the case of the TPSS and SCAN functionals. With TASK and HLE17, differences in the range 0.1–0.2 eV are obtained for some cases. For ZnS with TASK and for a number of cases with HLE17 it was necessary to improve the flexibility of the basis set by adding HDLOs (indicated with an asterisk in Table IV). For these cases, a warning occurs because the radial basis functions inside the atomic spheres are inaccurate. This warning is given when the

TABLE IV. Influence on MGGA band gaps of the chosen GGA potential (PBE or the optimal one) to calculate the core electrons and radial functions  $f_{\mu\ell m}$ . The optimal potential is RPBE for TPSS and SCAN, mRPBE for HLE17, and HCTH/407 for TASK. A positive value means that the band gap with the optimal GGA potential is smaller. For entries with an asterisk, we needed to add additional basis functions (in the form of HDLOs) to properly converge the calculations (see the text and Sec. II A for details). The values are in eV.

Solid	TPSS(PBE-RPBE)	SCAN(PBE-RPBE)	HLE17(PBE-mRPBE)	TASK(PBE-HCTH/407)
Al <sub>2</sub> O <sub>3</sub>	-0.01	-0.01	0.01	0.00
AlAs	-0.00	-0.00	0.05	-0.02
AlN	-0.00	-0.00	-0.03	0.00
AIP	-0.00	-0.00	0.08	0.00
AlSb	-0.00	0.00	-0.02	-0.01
Ar	-0.01	-0.01	0.15	-0.00
BeO	-0.00	-0.01	0.01*	-0.00
BN	-0.00	-0.00	0.03	-0.01
BP	-0.00	-0.00	0.07	0.01
C	-0.00	-0.00	0.01	-0.00
CaF <sub>2</sub>	-0.02	-0.02	0.14*	0.13
CaO	-0.01	-0.01	0.06*	0.03
CdSe	-0.00	-0.00	0.05*	0.01
GaAs	-0.00	-0.01	0.02*	0.01
GaP	-0.00	-0.00	0.04*	0.01
Ge	-0.01	-0.00	0.00	-0.01
InP	-0.01	-0.00	-0.02*	-0.00
KCl	-0.01	-0.01	0.01*	0.02
Kr	-0.01	-0.01	0.12	0.05
LiCl	-0.01	-0.01	0.06	0.02
LiF	-0.02	-0.02	0.02*	0.05
LiH	0.00	0.00	-0.00	-0.00
MgO	-0.01	-0.01	0.02*	0.02
NaCl	-0.01	-0.01	0.02*	0.02
NaF	-0.02	-0.02	0.00*	0.06
Ne	-0.01	-0.01	0.15*	0.14
Si	-0.00	-0.00	0.09	0.01
SiC	-0.00	-0.00	0.06	-0.01
ZnO	0.01	0.00	0.12*	0.22
ZnS	0.00	0.00	0.17*	0.11*

linearizing term  $\dot{u}_\ell$  of the basis function contributes a larger fraction of the charge density than expected (more than a few percent). When the radial basis functions are accurate, the radial solution  $u_\ell$  (or linear combinations thereof) will be very close to the KS orbitals, such that the contribution from the linearizing term stays small. We would like to stress that these warnings are given automatically and are a standard warning (in the WIEN2K code) that is used to diagnose badly chosen parameters (like atomic sphere size or energy parameters) or ghost bands.

As mentioned above, Ref. [71] reports band gaps calculated non-self-consistently with MGGA functionals. The orbitals (and thus the electron density) were generated by a GGA potential and then plugged into the total MGGA energy  $E_{\text{tot}}$  to calculate the band gap with  $E_g^{I-A} = I(N) - A(N) = [E_{\text{tot}}(N-1) - E_{\text{tot}}(N)] - [E_{\text{tot}}(N) - E_{\text{tot}}(N+1)]$ . By doing so, the agreement with the self-consistent VASP results is quite accurate provided that the optimal GGA orbitals are used. However, this method may be more cumbersome than the self-consistent implementation considered here. It may also be less accurate when the orbitals found using the GGA potential differ strongly from the self-consistent MGGA ones, which can be seen in the variational energies. Additionally,

the agreement with VASP is not as good as when the calculations are done self-consistently. Indeed, non-self-consistently the MADs with respect to VASP results are (in eV) 0.06 (for TPSS), 0.10 (for SCAN), 0.10 (for HLE17), and 0.20 (for TASK). These MADs are larger than those from Table III that are in the range 0.03–0.07 eV.

In summary, the band gaps obtained with our self-consistent implementation of the MGGA functionals in the WIEN2K code are in excellent agreement with the results obtained with the VASP code. This gives us confidence about the reliability of the implementation in terms of correctness and accuracy.

## B. Magnetism

In addition to the electronic band structure, magnetism is another property that can also be used to check the correctness of the implementation of the MGGA potential. In a previous work [72], the spin magnetic moment  $\mu_S$  of ferromagnetic (FM) and antiferromagnetic (AFM) solids was calculated with numerous MGGA functionals. However, due to the unavailability of the self-consistent MGGA implementation,  $\mu_S$  was calculated using the fixed spin-moment (FSM) [108] and



TABLE V. Spin magnetic moment  $\mu_S$  in FM (in  $\mu_B$  and per formula unit) and AFM (in  $\mu_B$  and inside the atomic volume of the transition-metal atom defined according to the Bader volume) solids calculated with MGGGA functionals using the WIEN2K code. The columns  $\Delta$  show the difference with respect to the value from Ref. [72] calculated without the self-consistent MGGGA potential, but with the FSM (for FM solids) or *C*-shift (for AFM solids) method, and a negative value means that the value from the FSM/*C*-shift method is larger. For comparison, the PBE results are also shown.

Solid	PBE	TPSS	$\Delta$	SCAN	$\Delta$	HLE17	$\Delta$	TASK	$\Delta$
FM									
Fe	2.22	2.23	0.00	2.60	-0.03	2.67	0.00	2.76	0.01
Co	1.62	1.65	0.00	1.77	-0.02	1.72	0.00	1.84	0.01
Ni	0.64	0.66	0.00	0.77	0.01	0.65	0.00	0.78	0.02
AFM									
MnO	4.40	4.42	0.01	4.52	-0.01	4.63	0.01	4.63	0.00
FeO <sup>a</sup>	NA	3.49	NA	3.57 <sup>c</sup>	NA	3.63 <sup>c</sup>	0.00	3.68 <sup>c</sup>	NA
FeO <sup>b</sup>	3.48	3.51 <sup>c</sup>	-0.01	3.60	-0.02	3.65	0.00	3.69	-0.01
CoO	2.45	2.51	0.01	2.61	0.01	2.64	0.01	2.65	-0.02
NiO	1.37	1.46	0.00	1.61	0.01	1.56	0.00	1.60	0.00

<sup>a</sup>Solution with a band gap.

<sup>b</sup>Solution with no band gap.

<sup>c</sup>Predicted ground state.

*C*-shift methods for FM and AFM systems, respectively. In both methods, the total energy  $E_{\text{tot}}$  [Eq. (13)] is minimized with respect to the magnitude of the moment  $\mu_S$  (which is varied within a certain range), and the value of  $\mu_S$  at the minimum of  $E_{\text{tot}}$  is the value that should in principle correspond to the value calculated self-consistently. In Ref. [72], the orbitals were calculated using the optimal GGA potentials (the same as those used in the present work), and it was shown that in some cases it is of importance to use the optimal potential (instead of the standard PBE) in order to mitigate the error due to the non-self-consistent procedure.

Here, we compare the magnetic moments from Ref. [72] with those obtained self-consistently. Such a comparison was already done in Ref. [72] for TPSS and SCAN in the case of MnO, FeO, CoO, and NiO, however the self-consistent results were obtained with other codes (VASP [104] and GPAW [40,109]). Table V shows the WIEN2K self-consistent values of  $\mu_S$  for FM metals (Fe, Co, and Ni) and AFM insulators (MnO, FeO, CoO, and NiO) systems, and the value in the columns  $\Delta$  indicates the difference with respect to the results obtained with the FSM/*C*-shift methods [72]. Note that the atomic magnetic moments on the transition-metal atoms in the AFM solids are defined according to the Bader volume from the quantum theory of atoms in molecules, as implemented in the CRITIC2 code [110,111]. The agreement between the two ways of calculating  $\mu_S$  is excellent, which again should demonstrate that the MGGGA potential is implemented correctly into the WIEN2K code. The largest difference, obtained for Fe with SCAN, is only  $-0.03\mu_B$  (the negative sign indicates that the FSM value from Ref. [72] is larger). Compared to the *C*-shift method, the current self-consistent implementation has the large advantage of not needing to rely on the additional variational procedure to find the magnetic moments  $\mu_S$  for each atomic sphere, a process that would be especially complicated and expensive for a supercell calculation (e.g., surface or a system with a defect).

In the particular case of FeO, an important point should be noted. Depending on the functional, two different solutions

can be stabilized. They differ in the occupation of the Fe *3d* orbitals, one corresponding to a metallic character and the other to a state with a band gap. With LDA and most common GGAs, only the metallic state can be obtained. Both solutions can be obtained with GGAs having a large enhancement factor like AK13 [89] and (probably most) MGGAs. Table V shows the FeO results for both solutions. It is possible to obtain the metallic and nonmetallic states with the MGGAs in the case of self-consistent calculations. To obtain the nonmetallic state for FeO, we had to “manually” populate the correct spin-down  $a_{1g}$  instead of the  $e'_g$  orbital (for instance with a properly occupied density matrix in a GGA+U calculation) to open the gap [112], after which the MGGAs would converge and correctly predict this state as the ground state. When resuming a self-consistent cycle from a PBE calculation or from a superposition of atomic densities, we obtain a gapless state with all MGGAs considered here. This is not the case for CoO, where the MGGAs would converge to the correct gapped state independent of the starting point of the self-consistency cycle. Therefore, only one solution can be found for AFM CoO.

Despite several attempts, only the metallic state can be obtained with the *C*-shift method for TPSS, SCAN, and TASK. This example of FeO shows the limitations of using the FSM/*C*-shift method instead of doing the self-consistent calculation. Finally, it is interesting to note that the ground state is the nonmetallic state with SCAN, HLE17, and TASK, but the metallic one with TPSS. In the case of CoO, all four MGGAs lead to a nonmetallic ground state, while PBE predicts a metallic ground state. HLE17 yields the largest gap of 1.55 eV, followed by SCAN (1.16 eV), TASK (0.51 eV), and TPSS (0.42 eV). All of these values are still smaller than the experimental value of  $2.5 \pm 0.3$  eV [113].

Finally, a few words should be said about the comparison with experiment. As shown in Ref. [72], as well as in other works [101,102,114–117], SCAN and TASK lead to magnetic moments that are clearly larger than experiment for FM metals, while TPSS is rather similar to PBE (i.e., a very slight overestimation) and HLE17 is quite irregular. For the AFM

TABLE VI. Equilibrium lattice constant (in Å) of solids calculated self-consistently (SC) or non-self-consistently (NSC) with MGGA functionals. Indicated in parentheses is the GGA potential that is used for calculating the core electrons and radial functions  $f_{\mu\ell m}$  (for SC calculations) or for calculating the orbitals plugged into the MGGA functional (for NSC calculations). For comparison, the experimental values are 4.205 (Na), 6.043 (Cs), 5.412 (Si), 4.905 (Pb), 3.599 (Cu), 5.569 (NaCl), 5.640 (GaAs), 4.334 (FeO), and 2.659 ( $a$ ) and 4.863 ( $c$ ) (Zn) [118–120].

	TPSS				SCAN			
	SC(RPBE)	SC(PBE)	NSC(RPBE)	NSC(PBE)	SC(RPBE)	SC(PBE)	NSC(RPBE)	NSC(PBE)
Na	4.241	4.242	4.237	4.237	4.213	4.211	4.205	4.207
Cs	6.280	6.279	6.275	6.264	6.238	6.235	6.230	6.226
Si	5.458	5.458	5.457	5.457	5.435	5.436	5.433	5.435
Pb <sup>a</sup>	4.983	4.983	4.984	4.984	4.972	4.972	4.978	4.974
Pb <sup>b</sup>	4.983	4.983	4.983	4.983	4.976	4.976	4.979	4.975
Cu	3.576	3.576	3.577	3.576	3.558	3.558	3.556	3.557
NaCl	5.702	5.703	5.704	5.700	5.583	5.583	5.580	5.583
GaAs	5.711	5.711	5.711	5.711	5.658	5.658	5.653	5.657
FeO <sup>c</sup>	4.281	4.281	NA	NA	4.274	4.273	NA	NA
FeO <sup>d</sup>	4.274	4.274	4.274	4.274	4.259	4.259	4.268	4.269
Zn ( $a$ )	2.639	2.639	2.640	2.638	2.574	2.574	2.576	2.574
Zn ( $c$ )	4.727	4.727	4.725	4.733	4.988	4.989	4.971	4.975

	HLE17				TASK			
	SC(mRPBE)	SC(PBE)	NSC(mRPBE)	NSC(PBE)	SC(HCTH/407)	SC(PBE)	NSC(HCTH/407)	NSC(PBE)
Na	4.049	4.050	4.044	4.048	4.740	4.741	4.617	4.624
Cs	6.087	6.093	6.079	6.090	7.547	7.549	7.094	7.180
Si	5.257	5.256	5.255	5.249	5.531	5.534	5.519	5.523
Pb <sup>a</sup>	4.870	4.869	4.871	4.863	5.143	5.146	5.147	5.140
Pb <sup>b</sup>	4.870	4.870	4.870	4.860	5.143	5.147	5.144	5.138
Cu	3.510	3.510	3.510	3.485	3.601	3.597	3.600	3.591
NaCl	5.575	5.570	5.574	5.540	6.273	6.272	6.188	6.267
GaAs	5.553	5.552	5.552	5.540	5.755	5.760	5.750	5.747
FeO <sup>c</sup>	4.169	4.166	NA	NA	4.383	4.393	NA	NA
FeO <sup>d</sup>	4.151	4.148	4.149	4.150	4.365	4.374	4.362	4.360
Zn ( $a$ )	2.584	2.588	2.584	2.578	2.617	2.615	2.607	2.605
Zn ( $c$ )	4.655	4.687	4.655	4.627	5.131	5.131	5.131	5.125

<sup>a</sup>With the  $4f$  and  $5s$  subshells treated in the core.

<sup>b</sup>With the  $4f$  and  $5s$  subshells treated in the valence.

<sup>c</sup>Solution with a band gap.

<sup>d</sup>Solution with no band gap.

insulators, SCAN and TASK improve with respect to PBE, which strongly underestimates the atomic magnetic moment. Again, TPSS is similar to PBE, while HLE17 is irregular.

#### IV. LATTICE CONSTANT: EFFECT OF SELF-CONSISTENCY

This section presents the results for the equilibrium lattice constant of selected solids: Na, Cs, Si, Pb, Cu, NaCl, GaAs, FeO (both states with and without a band gap), ZnO, and Zn. As in Sec. III A for the band gap, the purpose is to illustrate the influence of the GGA potential for calculating the core orbitals and radial functions  $f_{\mu\ell m}$ . The results [see columns “SC” (self-consistent) in Table VI] show that using either PBE or the corresponding optimal potential has very little influence. The largest difference is found in the  $c$  lattice constant of Zn with HLE17, where the difference between SC(mRPBE) and SC(PBE) reaches 0.03 Å. This is an outlier, because the second largest differences reach only around 0.005 Å, and

they are obtained for Cs (with HLE17), NaCl (with HLE17), GaAs (with TASK), and FeO (with TASK). Thus, as in the case of the band gap, the choice of the GGA potential for the core electrons and radial functions (either the standard PBE or the variationally optimal one) is unimportant in the vast majority of cases. Note that two sets of calculations were done for Pb: with the  $4f$  and  $5s$  subshells treated either in the core (thus with a GGA potential) or in the valence (thus with the MGGA potential). The results are basically the same. This confirms again that the treatment of the core electrons with a suitable GGA potential is a good approximation.

Also shown in Table VI are the equilibrium lattice constants obtained non-self-consistently (“NSC” columns) using the orbitals generated either from the PBE potential or the optimal GGA one. For the insulating state of FeO, such a calculation is not possible (see the discussion in Sec. III B), and this is indicated with “NA” (not available) in Table VI. Such a NSC procedure for calculating the lattice constant, bulk modulus, or cohesive energy with MGGA functionals has

TABLE VII. Comparison of various functionals to experiment for the  $c/a$  ratio (in Å) and the unit cell volume (in Å<sup>3</sup>) of hcp Zn. For the MGGGA functionals, the values of SCF calculations using the optimal GGA for core and radial functions are used.

	LDA	PBE	TPSS	SCAN	Expt. <sup>a</sup>
$c/a$	1.844	1.902	1.791	1.937	1.829
vol.	27.12	30.49	28.51	28.62	29.77

<sup>a</sup>Reference [120].

been used in previous works (see, e.g., Refs. [121,122]). The GGA potential to generate the orbitals has a larger influence in some cases. This is expected since the GGA potential is applied to all electrons, and not only to the core electrons as for SC calculations. The influence of the GGA potential on the lattice constant reaches 0.08 Å for Cs and NaCl, both with TASK. With TPSS and SCAN the GGA potential has a small influence, while non-negligible differences are seen with HLE17.

To obtain these results for Cu with HLE17 (PBE), Zn with TASK (NSCF on PBE and HCTH/407), and FeO with HLE17 (both GGAs), it was necessary to add HDLOs to the basis set in order to reduce the linearization error [50]. Without these additional basis functions, the WIEN2K code generated the same warnings as described in Sec. III A; the variational energy was higher and the result was much farther away from the proper one obtained with HLE17 (mRPBE). This shows again that in some cases, the addition of HDLOs can mitigate the use of a less-than-optimal GGA potential for the construction of the radial basis functions.

Comparing now the SC and NSC results, very large differences are obtained in the case of the TASK functional. For Na, Cs, and NaCl, the differences are about 0.1, 0.5, and 0.09 Å, respectively. With TPSS and SCAN, the differences between the NSC and SC results are very small. In the vast majority of cases, using the orbitals generated from the optimal GGA potential (instead of the PBE one) leads to the best agreement with the SC results. Clear exceptions are Na, Cs, and NaCl with TASK.

As a side comment, we mention that SCAN is one of the most accurate functionals for the lattice constant of solids, while TPSS is slightly less accurate and shows a (moderate) tendency to overestimate the values [121,122]. The two other functionals provide inconsistent results. While it is quite accurate in some cases (Zn and GaAs), HLE17 leads to some large underestimations [Na, Zn ( $c$ )] [74], while TASK leads to huge overestimations (Na, Cs), as shown in Table VI.

For the particular case of Zn, it is interesting to compare the results of the generally better-performing MGGAs (HLE17 and TASK severely over- and underbind, respectively) with the LDA and PBE functionals in Table VII. Compared to LDA, all three functionals improve upon the underestimation of the volume. However, both PBE and SCAN sacrifice the accurately predicted  $c/a$  ratio of LDA. TPSS does yield more accurate values for both the  $c/a$  ratio and the unit-cell volume.

We finish by comparing in Table VIII our SCAN lattice constants with the results from Refs. [122] and [123] that were obtained with the FHI-AIMS [124] (non-self-consistently using PBE orbitals) and VASP (self-consistently) codes, respectively. The agreement with the FHI-AIMS code is excellent, while sizable differences occur with VASP, in particular for NaCl.

## V. APPLICATION: ELECTRIC FIELD GRADIENT

As a final application of the MGGGA functionals, we discuss the calculation of the EFG [52]. We consider here the transition-metal atom in the elemental metals and Cu-compounds listed in Table IX. These are the same systems that we considered in a previous work [125], where we showed that among a plethora of methods, the GLLB-SC potential [126,127] leads overall to the best agreement with experiment. The screened hybrid functional HSE06 [22,128] was shown to be also rather good overall in comparison to the other methods. From the results shown in Table IX, it is clear that GLLB-SC is still the most accurate method for EFG calculations. It is close to the experimental value in all but one case, which is CuO.

For all other methods (which includes both the GGAs and the MGGAs) the results are mixed. We find for each of them three or four cases that have a large disagreement with experiment. The errors are not very systematic. For example, SCAN overestimates the EFG for Cd, but it underestimates the EFG of Cu<sub>2</sub>O. One trend that can be observed is that SCAN always leads to similar or larger values for the EFG compared to its “predecessors” PBE and TPSS. This suggests that the ground-state density with SCAN has an increased asphericity.

CuO and Cu<sub>2</sub>O are systems for which the standard LDA and PBE functionals lead to qualitatively wrong results, with values that are between two and four times smaller than experiment. It was shown [125,129] that HSE06 (for CuO and Cu<sub>2</sub>O) and GLLB-SC (for Cu<sub>2</sub>O) substantially improve the results. A few other semilocal methods also improve the predicted EFG value for Cu<sub>2</sub>O [125]. The results of the present work show that SCAN and TASK are accurate only for one or the other (CuO for SCAN and Cu<sub>2</sub>O for TASK), while HLE17 leads to reasonable EFG values for both compounds.

## VI. SUMMARY

In summary, the self-consistent implementation of MGGGA functionals into the WIEN2K code, which is based on an all-electron APW based method, has been presented. The formalism has been discussed in detail, and a comparison with results from the literature for the band gap of 30 solids shows very good agreement between the implementations. Magnetism has also been considered, and the magnetic moments obtained self-consistently are basically the same as those obtained non-self-consistently with the FSM/C-shift method, thus again showing that the new self-consistent implementation is reliable.

Then, the effect due to self-consistency on the lattice constant was revealed to be rather minor for the TPSS, SCAN, and HLE17 functionals, but very large in some cases like Cs or NaCl with the TASK functional. Finally, the EFG has been

TABLE VIII. Comparison of the SCAN equilibrium lattice constants (in Å) calculated with different codes.

Solid	WIEN2K-SC(RPBE)	FHI-AIMS <sup>a</sup>	VASP <sup>b</sup>
Na	4.211	4.207	4.193
Cs	6.235	NA	6.227
Si	5.436	5.433	5.429
Cu	3.558	3.558	3.566
NaCl	5.583	5.585	5.563
GaAs	5.658	5.656	5.659

<sup>a</sup>Reference [122].<sup>b</sup>Reference [123].

considered as an application. It has been shown that some of the MGGAs are quite accurate for CuO and Cu<sub>2</sub>O, which are very difficult cases for standard GGAs.

A technical but rather important point concerned the GGA potential that is used to calculate the core states and radial components of the basis functions. A choice for the GGA potential has to be made, and it is recommended to use the one that is, for a given MGA, the variationally optimal one. However, we have shown that using the standard PBE GGA potential leads to the same results in the vast majority of cases.

Thus, this new implementation of MGA functionals is accurate (since they are implemented in an all-electron code) and leads to reliable results. It uses the gKS scheme and is computationally barely more expensive as other common semilocal methods like LDA or GGAs. Finally, we also mention that the implementation has recently been used for the calculation of the band gap of 2D materials in Refs. [79,130].

### ACKNOWLEDGMENTS

J.D. and P.B. acknowledge support from the Austrian Science Fund (FWF) for Project No. W1243 (Solids4Fun). We are grateful to Miguel A. L. Marques for useful discussions regarding Libxc and the VASP calculations.

### APPENDIX A: MULTIPLICATIVE PART OF THE MGA POTENTIAL

The developed expression of  $\nabla \cdot (\partial \epsilon_{xc} / \partial \nabla \rho_\sigma)$  in Eq. (6) can be obtained by applying the chain rule. Where  $\xi = (\sigma, \sigma')$

TABLE IX. EFG (in  $10^{21}$  V/m<sup>2</sup>) on a transition-metal atom in elemental metals and CuO, Cu<sub>2</sub>O, and Cu<sub>2</sub>Mg calculated with MGA functionals at experimental lattice constants. For comparison, results from Ref. [125] obtained with the PBE, GLLB-SC, and HSE06 methods are also shown. The error bars of the experimental values are calculated from the uncertainty in the quadrupole moment and quadrupole coupling constants when available. The values that show large errors are underlined.

Method	Ti	Zn	Zr	Tc	Ru	Cd	CuO	Cu <sub>2</sub> O	Cu <sub>2</sub> Mg
PBE	1.73	3.49	4.19	-1.61	<u>-1.46</u>	7.54	<u>-2.83</u>	<u>-5.54</u>	-5.70
TPSS	1.69	3.33	4.20	-1.60	<u>-1.38</u>	7.36	<u>-3.74</u>	<u>-5.60</u>	-5.69
SCAN	1.75	<u>4.38</u>	4.37	-2.03	<u>-1.66</u>	<u>9.47</u>	-7.15	<u>-6.41</u>	-5.70
HLE17	1.70	<u>3.50</u>	<u>3.83</u>	<u>-0.93</u>	-0.73	7.44	-6.33	-8.59	<u>-4.76</u>
TASK	1.76	<u>4.77</u>	4.72	-1.66	<u>-1.42</u>	<u>10.33</u>	<u>-3.03</u>	-9.56	-5.78
GLLB-SC	1.62	3.72	4.42	-1.66	-1.26	8.05	<u>-4.65</u>	-9.99	-5.58
HSE06	1.5	<u>4.4</u>	4.5	-2.0	<u>-1.3</u>	<u>9.4</u>	-8.9	-8.3	<u>-6.3</u>
Expt. <sup>a</sup>	1.57(12)	3.40(35)	4.39(15)	1.83(9)	0.97(11)	7.60(75)	7.55(52)	10.08(69)	5.76(39)

<sup>a</sup>Reference [125].

is a shorthand index, it is given by

$$\begin{aligned}
\nabla \cdot \frac{\partial \epsilon_{xc}}{\partial \nabla \rho_\sigma} &= \sum_{\sigma' \sigma''}^{\uparrow \downarrow} (1 + \delta_{\sigma \sigma'}) \frac{\partial \epsilon_{xc}}{\partial \gamma_{\sigma \sigma'}} \rho_{\sigma''} \gamma_{\sigma' \sigma''} \\
&+ \sum_{\sigma'}^{\uparrow \downarrow} \sum_{\xi}^{\uparrow \uparrow, \uparrow \downarrow, \downarrow \downarrow} (1 + \delta_{\sigma \sigma'}) \frac{\partial \epsilon_{xc}}{\partial \gamma_{\sigma \sigma'}} \gamma_{\xi} \nabla \rho_{\sigma'} \cdot \nabla \gamma_{\xi} \\
&+ \sum_{\sigma'}^{\uparrow \downarrow} (1 + \delta_{\sigma \sigma'}) \frac{\partial \epsilon_{xc}}{\partial \gamma_{\sigma \sigma'}} \nabla^2 \rho_{\sigma'} \\
&+ \sum_{\sigma' \sigma''}^{\uparrow \downarrow} (1 + \delta_{\sigma \sigma'}) \frac{\partial \epsilon_{xc}}{\partial \gamma_{\sigma \sigma'}} \tau_{\sigma''} \nabla \rho_{\sigma'} \cdot \nabla \tau_{\sigma''}, \quad (A1)
\end{aligned}$$

where  $\delta_{\sigma \sigma'}$  is the Kronecker delta.  $\gamma_{\sigma \sigma'} = \nabla \rho_{\sigma'} \cdot \nabla \rho_{\sigma'}$  is the contracted density gradient that needs to be provided to Libxc [5,6], along with the electron density  $\rho_{\sigma}$  and the KED  $\tau_{\sigma}$ . The output provided by Libxc is the exchange-correlation energy density  $\epsilon_{xc}$  and its (partial) derivatives. Note that due to the  $\tau_{\sigma}$ -dependency of  $\epsilon_{xc}$ , there is an additional term [the last one in Eq. (A1)] compared to the GGA case.

### APPENDIX B: DERIVATION OF THE MATRIX ELEMENT $\langle \phi_{\mu} | \hat{v}_{\tau} | \phi_{\nu} \rangle$

The KED-derived matrix element is evaluated using integration by parts. When  $\phi_{\nu}$  is an APW+lo basis function, a surface term must be included due to the discontinuity of the

gradient  $\nabla\phi_v$  across the sphere boundary [61],

$$\langle\phi_\mu|\hat{v}_\tau|\phi_v\rangle = \frac{1}{2}\left[\sum_\alpha\int_{S_\alpha} + \int_1\right]v_\eta\nabla\phi_\mu^*\cdot\nabla\phi_v d^3\mathbf{r} - \frac{1}{2}\sum_\alpha\oint_{\partial S_\alpha}v_\eta\phi_\mu^*(\nabla\phi_v\cdot\hat{\mathbf{r}})d\Omega. \quad (\text{B1})$$

We consider the spherical term (volume integral over the sphere  $S_\alpha$ ), the surface term (integral over the sphere boundary  $\partial S_\alpha$ ), and the interstitial term separately.

### 1. Spherical term

In the spheres, all quantities like the basis functions and the potentials are expanded in spherical harmonics, allowing for a separation of variables. The gradient of the basis functions  $\phi_\mu = \sum_{\ell m} f_{\mu\ell m} Y_{\ell m}$  is most conveniently expressed using vector spherical harmonics [131, 132]:

$$\nabla\phi_\mu = \sum_{\ell m}\sqrt{\frac{\ell}{2\ell+1}}\left\{\frac{\partial}{\partial r} + \frac{\ell+1}{r}\right\}f_{\mu\ell m}\mathbf{Y}_{\ell m}^{\ell-1} - \sqrt{\frac{\ell+1}{2\ell+1}}\left\{\frac{\partial}{\partial r} - \frac{\ell}{r}\right\}f_{\mu\ell m}\mathbf{Y}_{\ell m}^{\ell+1}. \quad (\text{B2})$$

The vector spherical harmonics can be defined in different bases; for our purpose, the spherical basis

$$\hat{\mathbf{e}}_{+1} = \frac{-1}{\sqrt{2}}(\hat{\mathbf{e}}_x + i\hat{\mathbf{e}}_y), \quad (\text{B3})$$

$$\hat{\mathbf{e}}_0 = \hat{\mathbf{e}}_z, \quad (\text{B4})$$

$$\hat{\mathbf{e}}_{-1} = \frac{1}{\sqrt{2}}(\hat{\mathbf{e}}_x - i\hat{\mathbf{e}}_y) \quad (\text{B5})$$

is convenient. The vector spherical harmonics are then

$$\mathbf{Y}_{JM}^L = \sum_{\gamma}^{-1,0,1} C_{LM-\gamma\ 1\ \gamma}^{JM} Y_{LM-\gamma} \hat{\mathbf{e}}_{\gamma}, \quad (\text{B6})$$

where  $C_{\alpha\beta\gamma\delta}^{\epsilon\zeta}$  are Clebsch-Gordan coefficients. The dot product of two vector spherical harmonics with differing quantum numbers is given by

$$\mathbf{Y}_{J_1 M_1}^{*L_1} \cdot \mathbf{Y}_{J_2 M_2}^{L_2} = \sum_{\mu} C_{L_1 M_1 - \mu\ 1\ \mu}^{J_1 M_1} C_{L_2 M_2 - \mu\ 1\ \mu}^{J_2 M_2} \times Y_{L_1 M_1 - \mu}^* Y_{L_2 M_2 - \mu}. \quad (\text{B7})$$

Then, the dot product of the gradients of two basis functions of Eq. (B2) can be partitioned in four terms each involving a dot product of vector spherical harmonics, coefficients involving  $\ell$  and  $m$ , and radial integrals with four contributions. The angular integrals of a product of three spherical harmonics can be performed analytically and are given by the Gaunt coefficients  $G_{\ell_1 m_1 \ell_2 m_2}^{LM}$ :

$$G_{\ell_1 m_1 \ell_2 m_2}^{LM} = \int Y_{LM}^* Y_{\ell_1 m_1} Y_{\ell_2 m_2} d\Omega. \quad (\text{B8})$$

The four associated radial parts each have four terms. These are performed numerically, and are given by

$$R_{--} = I_{LM}[f_1^* f_2' r^2] + (\ell_1 + 1)I_{LM}[f_1^* f_2' r] + (\ell_2 + 1)I_{LM}[f_1^* f_2 r] + (\ell_1 + 1)(\ell_2 + 1)I_{LM}[f_1^* f_2], \quad (\text{B9})$$

$$R_{-+} = I_{LM}[f_1^* f_2' r^2] + (\ell_1 + 1)I_{LM}[f_1^* f_2' r] - \ell_2 I_{LM}[f_1^* f_2 r] - \ell_2(\ell_1 + 1)I_{LM}[f_1^* f_2], \quad (\text{B10})$$

$$R_{+-} = I_{LM}[f_1^* f_2' r^2] - \ell_1 I_{LM}[f_1^* f_2' r] + (\ell_2 + 1)I_{LM}[f_1^* f_2 r] - \ell_1(\ell_2 + 1)I_{LM}[f_1^* f_2], \quad (\text{B11})$$

$$R_{++} = I_{LM}[f_1^* f_2' r^2] - \ell_1 I_{LM}[f_1^* f_2' r] - \ell_2 I_{LM}[f_1^* f_2 r] + \ell_1 \ell_2 I_{LM}[f_1^* f_2], \quad (\text{B12})$$

where  $f_1 = f_{\mu\ell_1 m_1}$ ,  $f_2 = f_{\nu\ell_2 m_2}$ , and  $I_{LM}$  is the integrated product with the angular component of the KED-derived part of the potential,

$$I_{LM}[g] = \int_0^{R_{\text{at}}} (v_\eta)_{LM}(r)g(r)dr. \quad (\text{B13})$$

The parentheses  $(\dots)_{LM}$  indicate the  $LM$  component of the spherical harmonics expansion, i.e.,  $v_\eta = \sum_{LM} (v_\eta)_{LM} Y_{LM}$ .

Putting together the four radial and angular parts with their coefficients results in the following expression for a single sphere:

$$\int_S v_\eta \nabla\phi_\mu^* \cdot \nabla\phi_v d^3\mathbf{r} = \sum_{\{\xi\}} \frac{1}{\sqrt{(2\ell_1+1)(2\ell_2+1)}} \times \left( \sqrt{\ell_1\ell_2} R_{--} C_{\ell_1-1\ m_1-\gamma\ 1\ \gamma}^{\ell_1\ m_1} C_{\ell_2-1\ m_2-\gamma\ 1\ \gamma}^{\ell_2\ m_2} G_{LM\ \ell_2-1\ m_2-\gamma}^{\ell_1-1\ m_1-\gamma} \right. \\ - \sqrt{\ell_1(\ell_2+1)} R_{-+} C_{\ell_1-1\ m_1-\gamma\ 1\ \gamma}^{\ell_1\ m_1} C_{\ell_2+1\ m_2-\gamma\ 1\ \gamma}^{\ell_2\ m_2} G_{LM\ \ell_2+1\ m_2-\gamma}^{\ell_1-1\ m_1-\gamma} \\ - \sqrt{\ell_2(\ell_1+1)} R_{+-} C_{\ell_1+1\ m_1-\gamma\ 1\ \gamma}^{\ell_1\ m_1} C_{\ell_2-1\ m_2-\gamma\ 1\ \gamma}^{\ell_2\ m_2} G_{LM\ \ell_2-1\ m_2-\gamma}^{\ell_1+1\ m_1-\gamma} \\ \left. + \sqrt{(\ell_1+1)(\ell_2+1)} R_{++} C_{\ell_1+1\ m_1-\gamma\ 1\ \gamma}^{\ell_1\ m_1} C_{\ell_2+1\ m_2-\gamma\ 1\ \gamma}^{\ell_2\ m_2} G_{LM\ \ell_2+1\ m_2-\gamma}^{\ell_1+1\ m_1-\gamma} \right). \quad (\text{B14})$$

To obtain the result for all atoms in the unit cell, this expression is multiplied by a phase factor  $e^{i(\mathbf{K}'-\mathbf{K})\cdot\mathbf{R}_\alpha}$  and summed over the atomic indices  $\alpha$ .

The spherical terms are implemented similarly to the non-spherical corrections in APW based methods. The main points are these. A list of quantum numbers obeying the Gaunt

selection rules should be constructed, otherwise the loop over six  $\ell, m$  combinations becomes too expensive. For the potential lattice, spherical harmonics are used to exploit the point symmetry of the atomic sites. Secondly, one should note that the radial integrals  $R_{\pm\pm}$  are only dependent on the azimuthal numbers of the basis functions  $\ell_1$  and  $\ell_2$ ; the  $m$ -dependent factor enters only through the matching coefficients  $A_{\ell m}^{\mathbf{K}}$ ,  $B_{\ell m}^{\mathbf{K}}$  which do not depend on the radial coordinate.

## 2. Interstitial term

The interstitial term is much simpler to evaluate since the gradient of the basis function is simply given by  $\nabla\phi_{\mathbf{K}} = i\mathbf{K}\phi_{\mathbf{K}}$ . The result is then

$$\int_{\mathbf{I}} v_{\eta} \nabla\phi_{\mu}^* \cdot \nabla\phi_{\nu} d^3\mathbf{r} = \frac{1}{\Omega} \int_{\text{cell}} \Theta(\mathbf{r}) v_{\eta}(\mathbf{r}) \mathbf{K} \cdot \mathbf{K}' e^{i(\mathbf{K}' - \mathbf{K}) \cdot \mathbf{r}} d^3\mathbf{r} \\ = \mathbf{K} \cdot \mathbf{K}' (\Theta v_{\eta})_{\mathbf{G}' - \mathbf{G}}, \quad (\text{B15})$$

where the parentheses  $(\dots)_{\mathbf{G}}$  indicate the Fourier expansion coefficients, and

$$\Theta(\mathbf{r}) = \begin{cases} 0, & \mathbf{r} \in S_{\alpha}, \\ 1, & \mathbf{r} \in \mathbf{I} \end{cases} \quad (\text{B16})$$

is the step function. The notation  $(\theta v_{\eta})_{\mathbf{G}' - \mathbf{G}}$  indicates that the step function is multiplied in direct space, avoiding an expensive convolution sum in reciprocal space [49].

## 3. Surface term

The surface term is nonzero for APW(+lo) basis functions with a discontinuous gradient across the sphere boundary. Inside the sphere, one has

$$\lim_{r \rightarrow R_{\text{at}}}^{-} \nabla\phi_{\mu}(\mathbf{r}) \cdot \hat{\mathbf{r}} = \sum_{\ell m} f'_{\mu\ell m} Y_{\ell m} \Big|_{r=R_{\text{at}}}, \quad (\text{B17})$$

whereas in the interstitial, by using the Rayleigh expansion,

$$\lim_{r \rightarrow R_{\text{at}}}^{+} \nabla\phi_{\mu}(\mathbf{r}) \cdot \hat{\mathbf{r}} = \sum_{\ell m} 4\pi i^{\ell} j'_{\ell}(Kr) Y_{\ell m}^*(\hat{\mathbf{K}}) Y_{\ell m}(\hat{\mathbf{r}}) \Big|_{r=R_{\text{at}}}, \quad (\text{B18})$$

where the prime indicates the radial derivative. We can then define the radial part of the expansion as

$$g_{\nu\ell m}(r) = 4\pi i^{\ell} j'_{\ell}(K_{\nu}r) Y_{\ell m}^*(\hat{\mathbf{K}}_{\nu}). \quad (\text{B19})$$

The resulting surface integral can then be performed analytically:

$$\oint_{\partial S_{\alpha}} v_{\eta} \phi_{\mu}^* (\nabla\phi_{\nu} \cdot \hat{\mathbf{r}}) d\Omega \\ = R_{\text{at}}^2 \sum_{\{\xi\}} (v_{\eta})_{LM} G_{LM}^{\ell_1 m_1 \ell_2 m_2} \\ \times \left( f_{\mu\ell_1 m_1}^* f'_{\nu\ell_2 m_2} - g_{\mu\ell_1 m_1}^* g'_{\nu\ell_2 m_2} \right) \Big|_{r=R_{\text{at}}}, \quad (\text{B20})$$

where we used the spherical harmonics addition theorem, and  $\sum_{\{\xi\}}$  signifies the sum over all angular numbers. Note that the surface term is not Hermitian. In the implementation, it is explicitly made Hermitian.

The surface term is generally very small, and it has a negligible effect on all the calculations considered in this work. We verified this by comparing well-converged LAPW and APW+lo calculations, and noting that the difference in all cases was negligible. For the vast majority of cases, the same is true when comparing APW+lo calculations including or excluding the surface term.

We have noticed that in a few cases, numerical problems arise with our implementation of the surface term. We could not point out a single cause for these problems, but they occur for the functionals with a larger MGGA enhancement factor (like HLE17 or TASK) when using a large plane-wave cutoff. Cases with a larger asphericity in the density and potential (like Si) are also more strongly affected. Additionally, due to the nature of the APW basis functions, the potential itself becomes discontinuous. This occurs in both the multiplicative and the nonmultiplicative parts and is a consequence of the functions only being matched in value and not in slope at the sphere boundary. Choosing smaller sphere sizes also helped mitigate these numerical issues.

Because calculations excluding the surface term are numerically more reliable, we chose not to include this surface term in the APW+lo calculations for the present work.

- [1] P. Hohenberg and W. Kohn, Inhomogeneous electron gas, *Phys. Rev.* **136**, B864 (1964).
- [2] W. Kohn and L. J. Sham, Self-consistent equations including exchange and correlation effects, *Phys. Rev.* **140**, A1133 (1965).
- [3] J. P. Perdew and K. Schmidt, Jacob's ladder of density functional approximations for the exchange-correlation energy, in *Density Functional Theory and its Application to Materials*, edited by V. Van Doren, C. Van Alsenoy, and P. Geerlings, AIP Conf. Proc. No. 577 (AIP, New York, 2001), p. 1.
- [4] J. P. Perdew, A. Ruzsinszky, J. Tao, V. N. Staroverov, G. E. Scuseria, and G. I. Csonka, Prescription for the design and selection of density functional approximations: More con-

straint satisfaction with fewer fits, *J. Chem. Phys.* **123**, 062201 (2005).

- [5] M. A. L. Marques, M. J. T. Oliveira, and T. Burnus, Libxc: A library of exchange and correlation functionals for density functional theory, *Comput. Phys. Commun.* **183**, 2272 (2012).
- [6] S. Lehtola, C. Steigemann, M. J. T. Oliveira, and M. A. L. Marques, Recent developments in libxc—A comprehensive library of functionals for density functional theory, *SoftwareX* **7**, 1 (2018).
- [7] N. Mardirossian and M. Head-Gordon, Thirty years of density functional theory in computational chemistry: An overview and extensive assessment of 200 density functionals, *Mol. Phys.* **115**, 2315 (2017).

- [8] S. H. Vosko, L. Wilk, and M. Nusair, Accurate spin-dependent electron liquid correlation energies for local spin density calculations: A critical analysis, *Can. J. Phys.* **58**, 1200 (1980).
- [9] J. P. Perdew and Y. Wang, Accurate and simple analytic representation of the electron-gas correlation energy, *Phys. Rev. B* **45**, 13244 (1992).
- [10] A. D. Becke, Density-functional exchange-energy approximation with correct asymptotic behavior, *Phys. Rev. A* **38**, 3098 (1988).
- [11] J. P. Perdew, K. Burke, and M. Ernzerhof, Generalized Gradient Approximation Made Simple, *Phys. Rev. Lett.* **77**, 3865 (1996).
- [12] T. Van Voorhis and G. E. Scuseria, A novel form for the exchange-correlation energy functional, *J. Chem. Phys.* **109**, 400 (1998).
- [13] J. Tao, J. P. Perdew, V. N. Staroverov, and G. E. Scuseria, Climbing the Density Functional Ladder: Nonempirical Meta-Generalized Gradient Approximation Designed for Molecules and Solids, *Phys. Rev. Lett.* **91**, 146401 (2003).
- [14] F. Della Sala, E. Fabiano, and L. A. Constantin, Kinetic-energy-density dependent semilocal exchange-correlation functionals, *Int. J. Quantum Chem.* **116**, 1641 (2016).
- [15] A. D. Becke, Density-functional thermochemistry. III. The role of exact exchange, *J. Chem. Phys.* **98**, 5648 (1993).
- [16] M. Ernzerhof and G. E. Scuseria, Assessment of the Perdew-Burke-Ernzerhof exchange-correlation functional, *J. Chem. Phys.* **110**, 5029 (1999).
- [17] C. Adamo and V. Barone, Toward reliable density functional methods without adjustable parameters: The PBE0 model, *J. Chem. Phys.* **110**, 6158 (1999).
- [18] D. Pines and D. Bohm, A collective description of electron interactions: II. Collective vs individual particle aspects of the interactions, *Phys. Rev.* **85**, 338 (1952).
- [19] D. C. Langreth and J. P. Perdew, The exchange-correlation energy of a metallic surface, *Solid State Commun.* **17**, 1425 (1975).
- [20] J. P. Perdew, J. A. Chevary, S. H. Vosko, K. A. Jackson, M. R. Pederson, D. J. Singh, and C. Fiolhais, Atoms, molecules, solids, and surfaces: Applications of the generalized gradient approximation for exchange and correlation, *Phys. Rev. B* **46**, 6671 (1992).
- [21] J. Sun, A. Ruzsinszky, and J. P. Perdew, Strongly Constrained and Appropriately Normed Semilocal Density Functional, *Phys. Rev. Lett.* **115**, 036402 (2015).
- [22] J. Heyd, G. E. Scuseria, and M. Ernzerhof, Hybrid functionals based on a screened coulomb potential, *J. Chem. Phys.* **118**, 8207 (2003).
- [23] J. P. Perdew, A. Ruzsinszky, G. I. Csonka, O. A. Vydrov, G. E. Scuseria, L. A. Constantin, X. Zhou, and K. Burke, Restoring the Density-Gradient Expansion for Exchange in Solids and Surfaces, *Phys. Rev. Lett.* **100**, 136406 (2008).
- [24] Y. Zhao and D. G. Truhlar, Construction of a generalized gradient approximation by restoring the density-gradient expansion and enforcing a tight Lieb-Oxford bound, *J. Chem. Phys.* **128**, 184109 (2008).
- [25] J. P. Perdew, A. Ruzsinszky, G. I. Csonka, L. A. Constantin, and J. Sun, Workhorse Semilocal Density Functional for Condensed Matter Physics and Quantum Chemistry, *Phys. Rev. Lett.* **103**, 026403 (2009).
- [26] E. Fabiano, L. A. Constantin, and F. Della Sala, Generalized gradient approximation bridging the rapidly and slowly varying density regimes: A PBE-like functional for hybrid interfaces, *Phys. Rev. B* **82**, 113104 (2010).
- [27] P. Haas, F. Tran, P. Blaha, and K. Schwarz, Construction of an optimal GGA functional for molecules and solids, *Phys. Rev. B* **83**, 205117 (2011).
- [28] T. Bredow and A. R. Gerson, Effect of exchange and correlation on bulk properties of MgO, NiO, and CoO, *Phys. Rev. B* **61**, 5194 (2000).
- [29] J. Muscat, A. Wander, and N. M. Harrison, On the prediction of band gaps from hybrid functional theory, *Chem. Phys. Lett.* **342**, 397 (2001).
- [30] J. K. Perry, J. Tahir-Kheli, and W. A. Goddard, Antiferromagnetic band structure of  $\text{La}_2\text{CuO}_4$ : Becke-3-Lee-Yang-Parr calculations, *Phys. Rev. B* **63**, 144510 (2001).
- [31] J. Heyd, J. E. Peralta, G. E. Scuseria, and R. L. Martin, Energy band gaps and lattice parameters evaluated with the Heyd-Scuseria-Ernzerhof screened hybrid functional, *J. Chem. Phys.* **123**, 174101 (2005).
- [32] P. Blaha, K. Schwarz, G. K. H. Madsen, D. Kvasnicka, J. Luitz, R. Laskowski, F. Tran, and L. D. Marks, *WIEN2k: An Augmented Plane Wave plus Local Orbitals Program for Calculating Crystal Properties* (Vienna University of Technology, Austria, 2018).
- [33] P. Blaha, K. Schwarz, F. Tran, R. Laskowski, G. K. H. Madsen, and L. D. Marks, WIEN2k: An APW+lo program for calculating the properties of solids, *J. Chem. Phys.* **152**, 074101 (2020).
- [34] R. Neumann, R. H. Nobes, and N. C. Handy, Exchange functionals and potentials, *Mol. Phys.* **87**, 1 (1996).
- [35] C. Adamo, M. Ernzerhof, and G. E. Scuseria, The meta-GGA functional: Thermochemistry with a kinetic energy density dependent exchange-correlation functional, *J. Chem. Phys.* **112**, 2643 (2000).
- [36] A. V. Arbuznikov, M. Kaupp, V. G. Malkin, R. Reviakine, and O. L. Malkina, Validation study of meta-GGA functionals and of a model exchange-correlation potential in density functional calculations of EPR parameters, *Phys. Chem. Chem. Phys.* **4**, 5467 (2002).
- [37] A. V. Arbuznikov and M. Kaupp, The self-consistent implementation of exchange-correlation functionals depending on the local kinetic energy density, *Chem. Phys. Lett.* **381**, 495 (2003).
- [38] J. Gräfenstein, D. Izotov, and D. Cremer, Avoiding singularity problems associated with meta-GGA (generalized gradient approximation) exchange and correlation functionals containing the kinetic energy density, *J. Chem. Phys.* **127**, 214103 (2007).
- [39] J. Sun, M. Marsman, G. I. Csonka, A. Ruzsinszky, P. Hao, Y.-S. Kim, G. Kresse, and J. P. Perdew, Self-consistent meta-generalized gradient approximation within the projector-augmented-wave method, *Phys. Rev. B* **84**, 035117 (2011).
- [40] L. Ferrighi, G. K. H. Madsen, and B. Hammer, Self-consistent meta-generalized gradient approximation study of adsorption of aromatic molecules on noble metal surfaces, *J. Chem. Phys.* **135**, 084704 (2011).
- [41] F. Zahariev, S. S. Leang, and M. S. Gordon, Functional derivatives of meta-generalized gradient approximation (meta-GGA) type exchange-correlation density functionals, *J. Chem. Phys.* **138**, 244108 (2013).

- [42] F. G. Eich and M. Hellgren, Derivative discontinuity and exchange-correlation potential of meta-GGAs in density-functional theory, *J. Chem. Phys.* **141**, 224107 (2014).
- [43] Z.-h. Yang, H. Peng, J. Sun, and J. P. Perdew, More realistic band gaps from meta-generalized gradient approximations: Only in a generalized Kohn-Sham scheme, *Phys. Rev. B* **93**, 205205 (2016).
- [44] J. C. Womack, N. Mardirossian, M. Head-Gordon, and C.-K. Skylaris, Self-consistent implementation of meta-GGA functionals for the ONETEP linear-scaling electronic structure package, *J. Chem. Phys.* **145**, 204114 (2016).
- [45] Y. Yao and Y. Kanai, Plane-wave pseudopotential implementation and performance of SCAN meta-GGA exchange-correlation functional for extended systems, *J. Chem. Phys.* **146**, 224105 (2017).
- [46] K. Reiter, F. Mack, and F. Weigend, Calculation of Magnetic Shielding Constants with meta-GGA Functionals Employing the Multipole-Accelerated Resolution of the Identity: Implementation and Assessment of Accuracy and Efficiency, *J. Chem. Theor. Comput.* **14**, 191 (2018).
- [47] Y. Yamamoto, C. M. Diaz, L. Basurto, K. A. Jackson, T. Baruah, and R. R. Zope, Fermi-Löwdin orbital self-interaction correction using the strongly constrained and appropriately normed meta-GGA functional, *J. Chem. Phys.* **151**, 154105 (2019).
- [48] O. K. Andersen, Linear methods in band theory, *Phys. Rev. B* **12**, 3060 (1975).
- [49] D. J. Singh and L. Nordström, *Planewaves, Pseudopotentials, and the LAPW Method*, 2nd ed. (Springer, New York, 2006).
- [50] F. Karsai, F. Tran, and P. Blaha, On the importance of local orbitals using second energy derivatives for d and f electrons, *Comput. Phys. Commun.* **220**, 230 (2017).
- [51] The ELK code.
- [52] P. Blaha, K. Schwarz, and P. H. Dederichs, First-principles calculation of the electric-field gradient in hcp metals, *Phys. Rev. B* **37**, 2792 (1988).
- [53] J. P. Desclaux, Hartree Fock Slater self consistent field calculations, *Comput. Phys. Commun.* **1**, 216 (1970).
- [54] J. P. Desclaux, A multiconfiguration relativistic DIRAC-FOCK program, *Comput. Phys. Commun.* **9**, 31 (1975).
- [55] I. Grant, Relativistic calculation of atomic structures, *Adv. Phys.* **19**, 747 (1970).
- [56] L.-H. Ye, Computation of the Kohn-Sham orbital kinetic energy density in the full-potential linearized augmented plane-wave method, *Phys. Rev. B* **91**, 075101 (2015).
- [57] C. F. V. Weizsäcker, Zur Theorie der Kernmassen, *Z. Phys.* **96**, 431 (1935).
- [58] L. H. Thomas, The calculation of atomic fields, *Math. Proc. Cambridge Philos. Soc.* **23**, 542 (1927).
- [59] E. Fermi, Un metodo statistico per la determinazione di alcune priorieta dell'atome, *R. Accad. Naz. Lincei* **6**, 602 (1927).
- [60] T. M. Maier, Y. Ikabata, and H. Nakai, Restoring the iso-orbital limit of the kinetic energy density in relativistic density functional theory, *J. Chem. Phys.* **151**, 174114 (2019).
- [61] E. Sjöstedt, L. Nordström, and D. J. Singh, An alternative way of linearizing the augmented plane-wave method, *Solid State Commun.* **114**, 15 (2000).
- [62] G. K. H. Madsen, P. Blaha, K. Schwarz, E. Sjöstedt, and L. Nordström, Efficient linearization of the augmented plane-wave method, *Phys. Rev. B* **64**, 195134 (2001).
- [63] G. Michalíček, M. Betzinger, C. Friedrich, and S. Blügel, Elimination of the linearization error and improved basis-set convergence within the FLAPW method, *Comput. Phys. Commun.* **184**, 2670 (2013).
- [64] D. D. Koelling and B. N. Harmon, A technique for relativistic spin-polarised calculations, *J. Phys. C* **10**, 3107 (1977).
- [65] J. C. Slater, Wave functions in a periodic potential, *Phys. Rev.* **51**, 846 (1937).
- [66] D. Singh, Ground-state properties of lanthanum: Treatment of extended-core states, *Phys. Rev. B* **43**, 6388 (1991).
- [67] M. Weinert, E. Wimmer, and A. J. Freeman, Total-energy all-electron density functional method for bulk solids and surfaces, *Phys. Rev. B* **26**, 4571 (1982).
- [68] R. T. Sharp and G. K. Horton, A variational approach to the unipotent many-electron problem, *Phys. Rev.* **90**, 317 (1953).
- [69] J. B. Krieger, Y. Li, and G. J. Iafrate, Construction and application of an accurate local spin-polarized Kohn-Sham potential with integer discontinuity: Exchange-only theory, *Phys. Rev. A* **45**, 101 (1992).
- [70] A. Seidl, A. Görling, P. Vogl, J. A. Majewski, and M. Levy, Generalized Kohn-Sham schemes and the band-gap problem, *Phys. Rev. B* **53**, 3764 (1996).
- [71] F. Tran, J. Doumont, P. Blaha, M. A. L. Marques, S. Botti, and A. P. Bartók, On the calculation of the bandgap of periodic solids with MGGA functionals using the total energy, *J. Chem. Phys.* **151**, 161102 (2019).
- [72] F. Tran, G. Baudesson, J. Carrete, G. K. H. Madsen, P. Blaha, K. Schwarz, and D. J. Singh, Shortcomings of meta-GGA functionals when describing magnetism, *Phys. Rev. B* **102**, 024407 (2020).
- [73] B. Hammer, L. B. Hansen, and J. K. Nørskov, Improved adsorption energetics within density-functional theory using revised Perdew-Burke-Ernzerhof functionals, *Phys. Rev. B* **59**, 7413 (1999).
- [74] P. Verma and D. G. Truhlar, HLE17: An improved local exchange–correlation functional for computing semiconductor band gaps and molecular excitation energies, *J. Phys. Chem. C* **121**, 7144 (2017).
- [75] A. D. Boese and N. C. Handy, A new parametrization of exchange–correlation generalized gradient approximation functionals, *J. Chem. Phys.* **114**, 5497 (2001).
- [76] T. Aschebrock and S. Kümmel, Ultranonlocality and accurate band gaps from a meta-generalized gradient approximation, *Phys. Rev. Research* **1**, 033082 (2019).
- [77] J. W. Furness, A. D. Kaplan, J. Ning, J. P. Perdew, and J. Sun, Accurate and numerically efficient  $r^2$ SCAN meta-generalized gradient approximation, *J. Phys. Chem. Lett.* **11**, 8208 (2020).
- [78] A. P. Bartók and J. R. Yates, Regularized SCAN functional, *J. Chem. Phys.* **150**, 161101 (2019).
- [79] F. Tran, J. Doumont, L. Kalantari, P. Blaha, T. Rauch, P. Borlido, S. Botti, M. A. L. Marques, A. Patra, S. Jana, and P. Samal, Bandgap of two-dimensional materials: Thorough assessment of modern exchange-correlation functionals, *J. Chem. Phys.* **155**, 104103 (2021).
- [80] F. Murphy-Armando, M. Brehm, P. Steindl, M. T. Lusk, T. Fromherz, K. Schwarz, and P. Blaha, Light emission from direct band gap germanium containing split-interstitial defects, *Phys. Rev. B* **103**, 085310 (2021).



- [81] L. D. Marks, Predictive mixing for density functional theory (and other fixed-point problems), *J. Chem. Theory Comput.* **17**, 5715 (2021).
- [82] P. Borlido, T. Aull, A. W. Huran, F. Tran, M. A. L. Marques, and S. Botti, Large-scale benchmark of exchange–correlation functionals for the determination of electronic band gaps of solids, *J. Chem. Theory Comput.* **15**, 5069 (2019).
- [83] P. Borlido, J. Schmidt, A. W. Huran, F. Tran, M. A. L. Marques, and S. Botti, Exchange-correlation functionals for band gaps of solids: Benchmark, reparametrization and machine learning, *npj Comput. Mater.* **6**, 96 (2020).
- [84] J. P. Perdew, R. G. Parr, M. Levy, and J. L. Balduz, Density-Functional Theory for Fractional Particle Number: Derivative Discontinuities of the Energy, *Phys. Rev. Lett.* **49**, 1691 (1982).
- [85] L. J. Sham and M. Schlüter, Density-Functional Theory of the Energy Gap, *Phys. Rev. Lett.* **51**, 1888 (1983).
- [86] E. Kraisler and L. Kronik, Fundamental gaps with approximate density functionals: The derivative discontinuity revealed from ensemble considerations, *J. Chem. Phys.* **140**, 18A540 (2014).
- [87] A. Görling, Exchange-correlation potentials with proper discontinuities for physically meaningful Kohn-Sham eigenvalues and band structures, *Phys. Rev. B* **91**, 245120 (2015).
- [88] J. P. Perdew, Density functional theory and the band gap problem, *Int. J. Quantum Chem. Quantum Chem. Symp.* **28**, 497 (1986).
- [89] R. Armiento and S. Kümmel, Orbital Localization, Charge Transfer, and Band Gaps in Semilocal Density-Functional Theory, *Phys. Rev. Lett.* **111**, 036402 (2013).
- [90] K. Finzel and A. I. Baranov, A simple model for the Slater exchange potential and its performance for solids, *Int. J. Quantum Chem.* **117**, 40 (2017).
- [91] P. Verma and D. G. Truhlar, HLE16: A local kohn–sham gradient approximation with good performance for semiconductor band gaps and molecular excitation energies, *J. Phys. Chem. Lett.* **8**, 380 (2017).
- [92] S. Kümmel and L. Kronik, Orbital-dependent density functionals: Theory and applications, *Rev. Mod. Phys.* **80**, 3 (2008).
- [93] W. Yang, A. J. Cohen, and P. Mori-Sánchez, Derivative discontinuity, bandgap and lowest unoccupied molecular orbital in density functional theory, *J. Chem. Phys.* **136**, 204111 (2012).
- [94] J. P. Perdew, W. Yang, K. Burke, Z. Yang, E. K. U. Gross, M. Scheffler, G. E. Scuseria, T. M. Henderson, I. Y. Zhang, A. Ruzsinszky, H. Peng, J. Sun, E. Trushin, and A. Görling, Understanding band gaps of solids in generalized Kohn–Sham theory, *Proc. Natl. Acad. Sci. (USA)* **114**, 2801 (2017).
- [95] J. M. Crowley, J. Tahir-Kheli, and W. A. Goddard, Resolution of the band gap prediction problem for materials design, *J. Phys. Chem. Lett.* **7**, 1198 (2016).
- [96] A. J. Garza and G. E. Scuseria, Predicting band gaps with hybrid density functionals, *J. Phys. Chem. Lett.* **7**, 4165 (2016).
- [97] F. Tran and P. Blaha, Accurate Band Gaps of Semiconductors and Insulators with a Semilocal Exchange-Correlation Potential, *Phys. Rev. Lett.* **102**, 226401 (2009).
- [98] D. Koller, F. Tran, and P. Blaha, Merits and limits of the modified Becke-Johnson exchange potential, *Phys. Rev. B* **83**, 195134 (2011).
- [99] F. Tran, J. Doumont, L. Kalantari, A. W. Huran, M. A. L. Marques, and P. Blaha, Semilocal exchange-correlation potentials for solid-state calculations: Current status and future directions, *J. Appl. Phys.* **126**, 110902 (2019).
- [100] Y. Zhang, D. A. Kitchaev, J. Yang, T. Chen, S. T. Dacek, R. A. Sarmiento-Pérez, M. A. L. Marques, H. Peng, G. Ceder, J. P. Perdew, and J. Sun, Efficient first-principles prediction of solid stability: Towards chemical accuracy, *npj Comput. Mater.* **4**, 9 (2018).
- [101] E. B. Isaacs and C. Wolverton, Performance of the strongly constrained and appropriately normed density functional for solid-state materials, *Phys. Rev. Materials* **2**, 063801 (2018).
- [102] S. Jana, A. Patra, and P. Samal, Assessing the performance of the Tao-Mo semilocal density functional in the projector-augmented-wave method, *J. Chem. Phys.* **149**, 044120 (2018).
- [103] P. Borlido, J. Doumont, F. Tran, M. A. L. Marques, and S. Botti, Validation of pseudopotential calculations for the electronic band gap of solids, *J. Chem. Theor. Comput.* **16**, 3620 (2020).
- [104] G. Kresse and J. Furthmüller, Efficient iterative schemes for ab initio total-energy calculations using a plane-wave basis set, *Phys. Rev. B* **54**, 11169 (1996).
- [105] P. E. Blöchl, Projector augmented-wave method, *Phys. Rev. B* **50**, 17953 (1994).
- [106] G. Kresse and D. Joubert, From ultrasoft pseudopotentials to the projector augmented-wave method, *Phys. Rev. B* **59**, 1758 (1999).
- [107] X. Gonze, B. Amadon, G. Antonius, F. Arnardi, L. Baguet, J.-M. Beuken, J. Bieder, F. Bottin, J. Bouchet, E. Bousquet, N. Brouwer, F. Bruneval, G. Brunin, T. Cavignac, J.-B. Charraud, W. Chen, M. Côté, S. Cottenier, J. Denier, G. Geneste *et al.*, The Abinitproject: Impact, environment and recent developments, *Comput. Phys. Commun.* **248**, 107042 (2020).
- [108] K. Schwarz and P. Mohn, Itinerant metamagnetism in YCO<sub>2</sub>, *J. Phys. F* **14**, L129 (1984).
- [109] J. Enkovaara, C. Rostgaard, J. J. Mortensen, J. Chen, M. Duřak, L. Ferrighi, J. Gavnholt, C. Glinsvad, V. Haikola, H. A. Hansen, H. H. Kristoffersen, M. Kuisma, A. H. Larsen, L. Lehtovaara, M. Ljungberg, O. Lopez-Acevedo, P. G. Moses, J. Ojanen, T. Olsen, V. Petzold *et al.*, Electronic structure calculations with GPAW: A real-space implementation of the projector augmented-wave method, *J. Phys.: Condens. Matter* **22**, 253202 (2010).
- [110] A. Otero-de-la-Roza, M. A. Blanco, A. M. Pendás, and V. Luaña, Critic: A new program for the topological analysis of solid-state electron densities, *Comput. Phys. Commun.* **180**, 157 (2009).
- [111] A. Otero-de-la-Roza, E. R. Johnson, and V. Luaña, Critic2: A program for real-space analysis of quantum chemical interactions in solids, *Comput. Phys. Commun.* **185**, 1007 (2014).
- [112] I. I. Mazin and V. I. Anisimov, Insulating gap in FeO: Correlations and covalency, *Phys. Rev. B* **55**, 12822 (1997).
- [113] J. van Elp, J. L. Wieland, H. Eskes, P. Kuiper, G. A. Sawatzky, F. M. F. de Groot, and T. S. Turner, Electronic structure of CoO, Li-doped CoO, and LiCoO<sub>2</sub>, *Phys. Rev. B* **44**, 6090 (1991).

- [114] M. Ekholm, D. Gambino, H. J. M. Jönsson, F. Tasnádi, B. Alling, and I. A. Abrikosov, Assessing the SCAN functional for itinerant electron ferromagnets, *Phys. Rev. B* **98**, 094413 (2018).
- [115] Y. Fu and D. J. Singh, Applicability of the Strongly Constrained and Appropriately Normed Density Functional to Transition-Metal Magnetism, *Phys. Rev. Lett.* **121**, 207201 (2018).
- [116] Y. Fu and D. J. Singh, Density functional methods for the magnetism of transition metals: SCAN in relation to other functionals, *Phys. Rev. B* **100**, 045126 (2019).
- [117] D. Mejía-Rodríguez and S. B. Trickey, Analysis of overmagnetization of elemental transition metal solids from the SCAN density functional, *Phys. Rev. B* **100**, 041113(R) (2019).
- [118] A. Belsky, M. Hellenbrandt, V. L. Karen, and P. Luksch, New developments in the Inorganic Crystal Structure Database (ICSD): Accessibility in support of materials research and design, *Acta Crystallogr. B* **58**, 364 (2002).
- [119] G. Bergerhoff, R. Hundt, R. Sievers, and I. D. Brown, The inorganic crystal structure data base, *J. Chem. Inf. Comput. Sci.* **23**, 66 (1983).
- [120] J. Nuss, U. Wedig, A. Kirfel, and M. Jansen, The structural anomaly of Zinc: Evolution of lattice constants and parameters of thermal motion in the temperature range of 40 to 500 K, *Z. Anorg. Allg. Chem.* **636**, 309 (2010).
- [121] F. Tran, J. Stelzl, and P. Blaha, Rungs 1 to 4 of DFT Jacob's ladder: Extensive test on the lattice constant, bulk modulus, and cohesive energy of solids, *J. Chem. Phys.* **144**, 204120 (2016).
- [122] G.-X. Zhang, A. M. Reilly, A. Tkatchenko, and M. Scheffler, Performance of various density-functional approximations for cohesive properties of 64 bulk solids, *New J. Phys.* **20**, 063020 (2018).
- [123] D. Mejía-Rodríguez and S. B. Trickey, Deorbitalized meta-GGA exchange-correlation functionals in solids, *Phys. Rev. B* **98**, 115161 (2018).
- [124] V. Blum, R. Gehrke, F. Hanke, P. Havu, V. Havu, X. Ren, K. Reuter, and M. Scheffler, *Ab initio* molecular simulations with numeric atom-centered orbitals, *Comput. Phys. Commun.* **180**, 2175 (2009).
- [125] F. Tran, S. Ehsan, and P. Blaha, Assessment of the GLLB-SC potential for solid-state properties and attempts for improvement, *Phys. Rev. Materials* **2**, 023802 (2018).
- [126] O. Gritsenko, R. van Leeuwen, E. van Lenthe, and E. J. Baerends, Self-consistent approximation to the Kohn-Sham exchange potential, *Phys. Rev. A* **51**, 1944 (1995).
- [127] M. Kuisma, J. Ojanen, J. Enkovaara, and T. T. Rantala, Kohn-Sham potential with discontinuity for band gap materials, *Phys. Rev. B* **82**, 115106 (2010).
- [128] A. V. Krugau, O. A. Vydrov, A. F. Izmaylov, and G. E. Scuseria, Influence of the exchange screening parameter on the performance of screened hybrid functionals, *J. Chem. Phys.* **125**, 224106 (2006).
- [129] F. Tran and P. Blaha, Implementation of screened hybrid functionals based on the Yukawa potential within the LAPW basis set, *Phys. Rev. B* **83**, 235118 (2011).
- [130] A. Patra, S. Jana, P. Samal, F. Tran, L. Kalantari, J. Doumont, and P. Blaha, Efficient band structure calculation of two-dimensional materials from semilocal density functionals, *J. Phys. Chem. C* **125**, 11206 (2021).
- [131] D. A. Varshalovich, A. N. Moskalev, and V. K. Khersonskii, *Quantum Theory of Angular Momentum* (World Scientific, Singapore, 1988).
- [132] G. B. Arfken, H. J. Weber, and F. E. Harris, *Mathematical Methods for Physicists*, 7th ed. (Elsevier Academic, San Diego, 2013).